

# A Physics-Informed, Global-in-Time Neural Particle Method for the Spatially Homogeneous Landau Equation

Minseok Kim<sup>1,†</sup>, Sung-Jun Son<sup>2,†</sup>, Yeoneung Kim<sup>1,\*</sup>, Donghyun Lee<sup>2,\*</sup>

<sup>1</sup>Department of Applied Artificial Intelligence, Seoul National University of Science and Technology, Seoul, Republic of Korea

<sup>2</sup>Department of Mathematical Sciences, Pohang University of Science and Technology (POSTECH), Pohang, Republic of Korea

<sup>†</sup>These authors contributed equally to this work.

<sup>\*</sup>Corresponding authors. YK: yeoneung@seoultech.ac.kr, DL: donglee@postech.ac.kr

## Abstract

We propose a physics-informed neural particle method (PINN-PM) for the spatially homogeneous Landau equation. The method adopts a Lagrangian interacting-particle formulation and jointly parameterizes the time-dependent score and the characteristic flow map with neural networks. Instead of advancing particles through explicit time stepping, the Landau dynamics is enforced via a continuous-time residual defined along particle trajectories. This design removes time-discretization error and yields a mesh-free solver that can be queried at arbitrary times without sequential integration. We establish a rigorous stability analysis in an  $L_v^2$  framework. The deviation between learned and exact characteristics is controlled by three interpretable sources: (i) score approximation error, (ii) empirical particle approximation error, and (iii) the physics residual of the neural flow. This trajectory estimate propagates to density reconstruction, where we derive an  $L_v^2$  error bound for kernel density estimators combining classical bias–variance terms with a trajectory-induced contribution. Using Hyvärinen’s identity, we further relate the oracle score-matching gap to the  $L_v^2$  score error and show that the empirical loss concentrates at the Monte Carlo rate, yielding computable a posteriori accuracy certificates. Numerical experiments on analytical benchmarks, including the two- and three-dimensional BKW solutions, as well as reference-free configurations, demonstrate stable transport, preservation of macroscopic invariants, and competitive or improved accuracy compared with time-stepping score-based particle and blob methods while using significantly fewer particles.

## 1 Introduction

The spatially homogeneous Landau equation models the evolution of the velocity distribution of charged particles undergoing grazing collisions. It describes the time evolution of the velocity distribution  $\tilde{f}_t(v)$ :<sup>1</sup>

$$\partial_t \tilde{f}_t(v) = \nabla_v \cdot \int_{\Omega} A(v - v^*) (\tilde{f}_t(v^*) \nabla_v \tilde{f}_t(v) - \tilde{f}_t(v) \nabla_{v^*} \tilde{f}_t(v^*)) dv^*, \quad v \in \Omega. \quad (1.1)$$

Here  $A(z) = C_\gamma |z|^\gamma (|z|^2 I - z \otimes z)$  for  $\gamma \in [-3, 1]$ . Equation (1.1) possesses a gradient–flow structure and conserves mass, momentum, and energy while dissipating entropy [21]. Numerically, the challenge lies in designing schemes that (i) capture this long–time structure, (ii) scale efficiently to high dimensions, and (iii) provide verifiable accuracy certificates.

**Mathematical and Numerical Background.** The mathematical study of the Landau equation dates back to the seminal work of Landau [16] and its derivation from the Boltzmann equation [7]. Analytical breakthroughs regarding weak solutions, regularity, and convergence to equilibrium have been established

<sup>1</sup>We focus on the Coulomb case  $\gamma = -3$ ; the Maxwell case  $\gamma = 0$  follows verbatim.

in works by Villani and Desvillettes [9, 10, 21, 22], with recent results addressing global regularity [12]. Translating these insights into robust numerical simulations has been a persistent challenge. Early structure-preserving efforts focused on conservation laws and entropy decay (e.g., entropy-consistent finite-volume and spectral solvers [2, 8, 17]). However, grid-based methods often struggle with the *curse of dimensionality*. As an alternative, particle-based approaches like Direct Simulation Monte Carlo (DSMC) [11] and Particle-In-Cell (PIC) variants [1, 6] were developed. While naturally mesh-less, they often suffer from statistical noise or require complex re-projection steps to maintain conservation. Recent works have also explored randomized interaction reductions such as the random batch method [4] and structure-preserving discretizations [13] (see also the survey in [5]).

**The Score-Based Particle (SBP) Paradigm.** A recent paradigm shift stems from re-interpreting the Landau equation as a gradient flow in the Wasserstein metric [3, 4]. This perspective links kinetic theory to score matching, a technique pioneered by Hyvärinen [15] and popularized in generative modeling [19, 20]. In this context, the velocity field’s nonlinearity is driven by the score  $s = \nabla \log f$ . Building on this, Huang and Wang proposed the score-based particle (SBP) methodology [14]. SBP learns the score dynamically to bypass expensive kernel density estimation (KDE) while advancing particles via a structure-preserving ODE. This method inherits conservation from deterministic particles, scales favorably with dimension (empirically  $\mathcal{O}(N)$ ), and provides theoretical links between the Kullback–Leibler divergence and the score-matching objective [14].

Despite these advances, SBP (and most particle formulations) still evolve trajectories via an explicit time loop. Consequently, accuracy and computational cost are tightly coupled to the time step  $\Delta t$ . Even with an exact score, one encounters Monte Carlo sampling error  $\mathcal{O}(N^{-1/2})$  and time discretization error  $\mathcal{O}(\Delta t)$ , making accuracy certification dependent on external time-step control. Moreover, existing SBP analyses typically rely on coercivity assumptions on the collision kernel to obtain entropy-based stability estimates. In contrast, our trajectory-based analysis only requires boundedness and Lipschitz regularity of the interaction kernel, as it relies on stability of the characteristic flow rather than entropy dissipation.

**Physics-Informed Neural Networks (PINNs).** Physics-Informed Neural Networks (PINNs) have emerged as a mesh-free paradigm for solving partial differential equations by embedding the governing equation directly into the training objective [18]. Instead of discretizing time and space explicitly, PINNs approximate the solution as a neural function and enforce the PDE through a continuous-time residual loss evaluated at collocation points. This approach has demonstrated effectiveness in high-dimensional settings, where traditional grid-based solvers suffer from the curse of dimensionality.

However, most existing PINN formulations operate in an Eulerian framework, where the density field itself is parameterized and the PDE residual is enforced pointwise. For nonlinear kinetic equations such as the Landau equation, this strategy faces two difficulties: (i) the collision operator is nonlocal and quadratic in the density, and (ii) characteristic transport plays a central structural role.

We propose a fundamentally different perspective. Instead of alternating between score learning and time stepping, we learn the entire interacting particle dynamics as a global-in-time neural flow. Concretely, we parameterize both the score  $s(v, t)$  and the characteristic map  $\Phi_\xi(v_0, t)$  as neural networks defined on  $(v, t)$ , and enforce the Landau dynamics through a continuous-time physics residual. Once trained, the model acts as a neural particle simulator: given initial samples  $V_i$ , particle configurations at arbitrary times are generated directly by neural inference, without sequential integration.

**Contributions.** We propose PINN-based particle method (PINN-PM) for solving the Landau equation and our main contributions are as follows:

- **Global-in-time neural interacting particle formulation.** We remove explicit time discretization by jointly learning the score and characteristic flow over the time horizon.
- **Neural particle simulator.** The learned flow map  $\Phi_\xi$  enables mesh-free temporal inference: particle configurations at arbitrary times are obtained through a single forward pass, without time stepping.
- **Residual-based error certificates.** We establish trajectory stability and density reconstruction bounds linking score error, measure mismatch, and physics residual to deployment-time accuracy.

Compared to SBP [14], our approach eliminates time-step dependence, provides end-to-end error guarantees directly tied to training losses, and empirically achieves competitive or improved accuracy with significantly fewer particles.

**Organization.** The remainder of this paper is organized as follows. Section 2 presents the problem formulation and the proposed PINN-PM methodology. Section 3 develops the stability and trajectory error analysis of the neural characteristic flow. Section 4 establishes an oracle-to-dynamics certification framework connecting score learning errors to Wasserstein stability and density reconstruction. Section 5 reports numerical experiments, and Section 6 concludes this paper.

**Notation :** To avoid confusion, we fix the following convention:

- We use  $|a|$  to denote the absolute value of a scalar  $a \in \mathbb{R}$ , and  $\|x\|$  to denote the Euclidean norm of a vector  $x \in \mathbb{R}^d$ . On the torus  $\mathbb{T}^d = \mathbb{R}^d/\mathbb{Z}^d$ , we also use  $\|x - y\|$  to denote the torus distance

$$\|x - y\| := \min_{k \in \mathbb{Z}^d} \|x - y + k\|.$$

- For a function  $f = f(v)$  defined on the  $d$ -dimensional torus  $\mathbb{T}^d$ , we write

$$\|f\|_{L_v^2} = \left( \int_{\mathbb{T}^d} |f(v)|^2 dv \right)^{1/2},$$

and, when  $f$  depends also on time  $t$ , we use the notation  $\|f_t\|_{L_v^2}$  to emphasize that the norm is taken only with respect to the velocity variable  $v$ .

- The expectation symbol  $\mathbb{E}[\cdot]$  without a subscript always refers to the expectation with respect to the randomness of particle sampling (Monte Carlo average) at time  $t = 0$ .

## 2 Problem formulation and deterministic particle approximation

### 2.1 Spatially homogeneous Landau equation

We consider the spatially homogeneous Landau equation in velocity space:

$$\partial_t \tilde{f}_t(v) = \nabla_v \cdot \int_{\Omega} A(v - v^*) (\tilde{f}_t(v^*) \nabla_v \tilde{f}_t(v) - \tilde{f}_t(v) \nabla_{v^*} \tilde{f}_t(v^*)) dv^*, \quad v \in \Omega, \quad (2.1)$$

where  $\Omega = \mathbb{R}^d$  or  $\mathbb{T}^d$  (see Remark 1), and

$$A(z) = C_\gamma |z|^\gamma (|z|^2 I - z \otimes z), \quad \gamma \in [-3, 1].$$

We focus on the Coulomb case  $\gamma = -3$  and the Maxwell case  $\gamma = 0$ .

**Remark 1** (Domain and Boundary Conditions). *We formulate the problem on the torus  $\Omega = \mathbb{T}^d$  to simplify the exposition of boundary terms. This choice avoids technical digressions on decay rates at infinity while retaining the core nonlinear structure of the collision operator. However, our analytical framework and the PINN formulation extend directly to the whole space  $\mathbb{R}^d$  under standard regularity and decay assumptions (i.e.,  $f_t(v)$  and an approximate score  $s_\theta(v, t)$  vanishing sufficiently fast as  $|v| \rightarrow \infty$  to validate integration-by-parts identities). Since the Landau operator is local in space (homogeneous) and nonlocal only in velocity, the distinction between  $\mathbb{T}^d$  and  $\mathbb{R}^d$  does not alter the essential methodology.*

Equation (2.1) admits the transport form

$$\partial_t \tilde{f}_t = -\nabla_v \cdot (\tilde{f}_t U[\tilde{f}_t]), \quad (2.2)$$

where the nonlinear velocity field is given by

$$U[\tilde{f}_t](v) = - \int_{\Omega} A(v - v^*) (\nabla_v \log \tilde{f}_t(v) - \nabla_{v^*} \log \tilde{f}_t(v^*)) \tilde{f}_t(v^*) dv^*. \quad (2.3)$$

Introducing the score function

$$\tilde{s}_t(v) := \nabla_v \log \tilde{f}_t(v),$$

the drift can be written compactly as

$$U[\tilde{f}_t](v) = - \int_{\Omega} A(v - v^*) (\tilde{s}_t(v) - \tilde{s}_t(v^*)) \tilde{f}_t(v^*) dv^*.$$

Thus, the spatially homogeneous Landau equation may be interpreted as a nonlinear transport equation in velocity space driven by a mean-field interaction expressed through score differences.

Under suitable regularity assumptions on  $\tilde{f}_t$ , the transport form (2.2) admits a Lagrangian representation. Let  $T_t : \Omega \rightarrow \Omega$  denote the characteristic flow defined by

$$\frac{d}{dt} T_t(v_0) = U[\tilde{f}_t](T_t(v_0)), \quad T_0(v_0) = v_0. \quad (2.4)$$

Then the solution of (2.2) can be written as the pushforward

$$\tilde{f}_t = T_t \# f_0, \quad (2.5)$$

in the sense that for any smooth test function  $\phi$ ,

$$\int_{\Omega} \phi(v) \tilde{f}_t(v) dv = \int_{\Omega} \phi(T_t(v_0)) f_0(v_0) dv_0.$$

This formulation highlights that the Landau equation can be interpreted as the mean-field limit of an interacting particle system in velocity space.

## 2.2 Deterministic interacting particle approximation

To approximate the pushforward representation (2.5), we consider  $N$  particles

$$\{v_t^{(i)}\}_{i=1}^N$$

initialized as i.i.d. samples from  $f_0$ .

The empirical measure is defined by

$$f_t = \frac{1}{N} \sum_{i=1}^N \delta_{v_t^{(i)}}. \quad (2.6)$$

Replacing the mean-field integral in (2.3) by its empirical approximation yields the deterministic interacting particle system

$$\frac{d}{dt} v_t^{(i)} = - \frac{1}{N} \sum_{j=1}^N A(v_t^{(i)} - v_t^{(j)}) (\tilde{s}_t(v_t^{(i)}) - \tilde{s}_t(v_t^{(j)})), \quad i = 1, \dots, N. \quad (2.7)$$

In practice, the exact score  $\tilde{s}_t$  is unknown. Classical deterministic particle methods therefore approximate the score either by kernel density estimation or by neural score matching.

A representative time-discrete scheme, as used in score-based particle methods, reads

$$v_{t_{n+1}}^{(i)} = v_{t_n}^{(i)} - \Delta t \frac{1}{N} \sum_{j=1}^N A(v_{t_n}^{(i)} - v_{t_n}^{(j)}) (s_{\theta}(v_{t_n}^{(i)}, t_n) - s_{\theta}(v_{t_n}^{(j)}, t_n)), \quad (2.8)$$

where  $s_{\theta}$  denotes a learned approximation of the score.

This formulation preserves the interacting particle structure but introduces two fundamental sources of numerical error:

- time discretization error of order  $\mathcal{O}(\Delta t)$ ,
- Monte Carlo sampling error of order  $\mathcal{O}(N^{-1/2})$ .

Moreover, the particle dynamics must be advanced sequentially in time, so that computational cost and accuracy remain coupled to the time-step size.

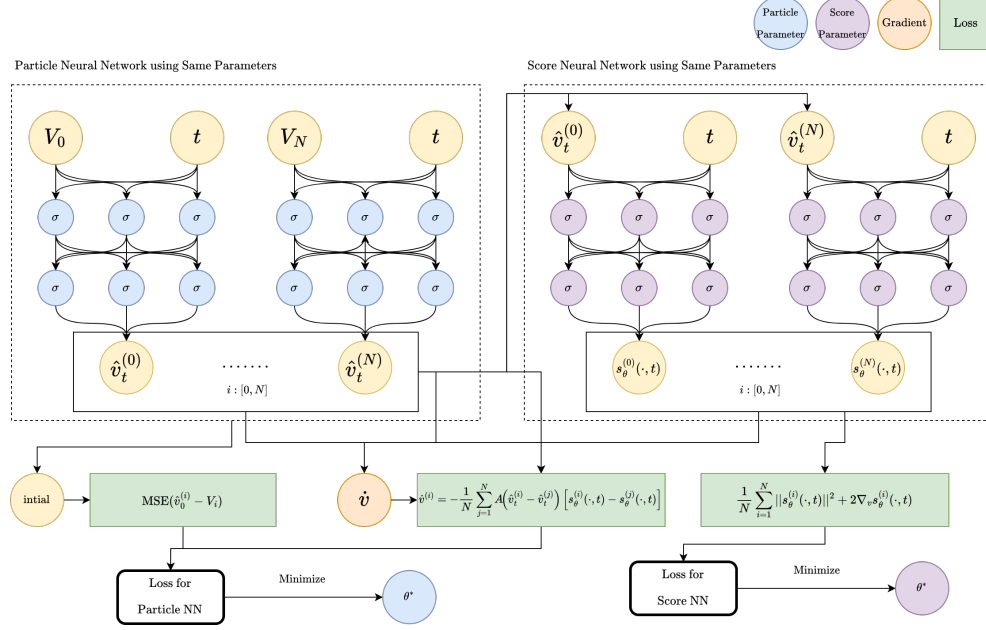


Figure 1: **Conceptual architecture of PINN-PM.** Left: global-in-time trajectory network  $\Phi_\xi$  (shared parameters across particles). Right: global-in-time score network  $s_\theta$ . Both networks are trained jointly through a physics residual enforcing the Landau characteristics and an implicit score-matching loss. The framework removes explicit time stepping and enables direct querying at arbitrary times.

### 2.3 Global-in-time Neural Parameterization

To overcome the limitations of discrete time-stepping, we propose the **PINN-PM** framework. The core idea is to parameterize both the particle trajectories and the score function as continuous functions of time, unifying density estimation and dynamics evolution into a single global-in-time optimization problem.

We introduce two neural networks shared across all particles and time instants:

- **Dynamics Network (Flow Map):**  $\Phi_\xi : \mathbb{R}^d \times [0, T] \rightarrow \mathbb{R}^d$ .

This network approximates the Lagrangian flow map  $v_t = T_t(v_0)$ . Given a set of initial particles  $\{V_i\}_{i=1}^N \sim f_0$ , the position of the  $i$ -th particle at any arbitrary time  $t$  is given explicitly by:

$$\hat{v}_t^{(i)} := \Phi_\xi(V_i, t). \quad (2.9)$$

This parameterization ensures that the empirical measure is defined continuously in time as  $f_t = \frac{1}{N} \sum_{i=1}^N \delta_{\Phi_\xi(V_i, t)}$ .

- **Score Network:**  $s_\theta : \mathbb{R}^d \times [0, T] \rightarrow \mathbb{R}^d$ .

This network approximates the time-dependent score function  $s_\theta(v, t) \approx \nabla_v \log f_t(v)$ . Unlike previous approaches that train separate models for each time step,  $s_\theta$  learns the score evolution over the entire horizon  $[0, T]$  simultaneously.

Figure 1 illustrates the overall architecture of the proposed PINN-PM. Unlike time-stepping particle methods, which repeatedly update particles and retrain the score, our framework jointly learns (i) a global-in-time trajectory network  $\Phi_\xi(V_i, t)$  and (ii) a global-in-time score network  $s_\theta(v, t)$ . The two networks are coupled through a physics residual enforcing the Landau characteristic equation and an implicit score-matching objective. This design eliminates explicit temporal discretization and enables mesh-free inference in time.

To implement the global-in-time parameterization in practice, we adopt a structured embedding design illustrated in Figure 2. The initial velocity  $V_i$  and time variable  $t$  are first mapped through separate embedding networks, producing velocity features  $E^{i,v}$  and time features  $E^{i,t}$ . These embeddings are subsequently fused and processed by shared hidden layers to produce the continuous-time output  $v_t^{(i)}$ .

This separation of velocity and time embeddings stabilizes training and improves representation capacity, while preserving the interpretation of  $\Phi_\xi$  as a global flow map defined over  $(v_0, t)$ .

A key consequence of this design is that, once trained, the network  $\Phi_\xi$  functions as a neural particle simulator. Given initial samples  $V_i$ , particle configurations at any time  $t$  are obtained via a single forward evaluation, without numerical integration. This contrasts fundamentally with time-stepping particle methods, which require sequential updates and incur  $\Delta t$ -dependent errors.

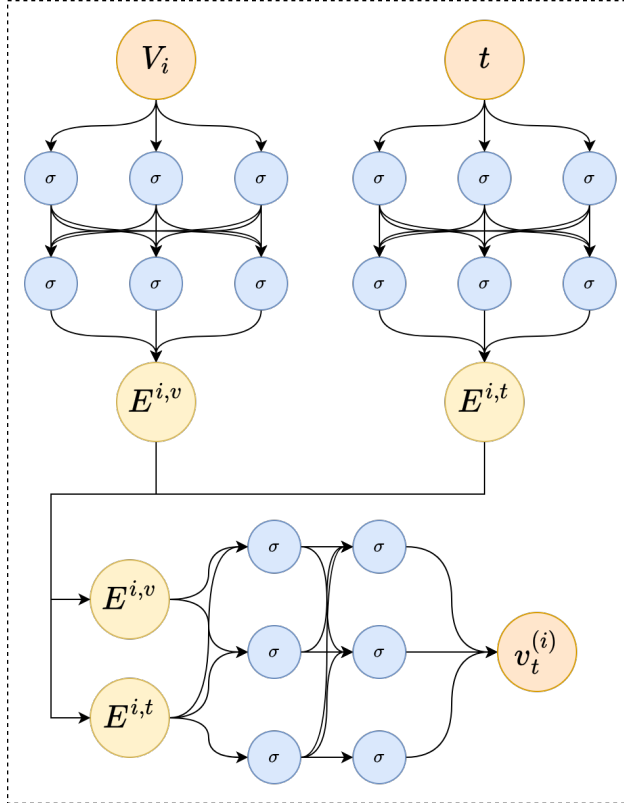


Figure 2: **Global-in-time architecture of PINN-PM.** Separate velocity and time embeddings are processed by neural blocks and fused to produce the continuous-time trajectory  $v_t^{(i)}$ . The architecture enables mesh-free querying in time without explicit time stepping.

## 2.4 Physics-Informed Global Flow Learning: Formulation and Algorithm

We now describe the unified training formulation of PINN-PM, which jointly learns the global characteristic flow and the time-dependent score without explicit time discretization.

We train the parameters  $(\xi, \theta)$  jointly by minimizing a composite loss function that enforces (i) statistical consistency of the score (via Implicit Score Matching) and (ii) physical consistency of the trajectories (via the Landau characteristic residual).

**(1) Implicit Score Matching (ISM) in Continuous Time.** Since the true density is unknown, we employ the Hyvärinen objective. For a batch of collocation times  $\{t_k\}_{k=1}^{N_t} \subset [0, T]$ , we minimize:

$$\hat{\mathcal{L}}_{\text{ISM},t}(s_\theta) = \frac{1}{N_t N} \sum_{k=1}^{N_t} \sum_{i=1}^N \left( \|s_\theta(v_{t_k}^{(i)}, t_k)\|^2 + 2\nabla_v \cdot s_\theta(v_{t_k}^{(i)}, t_k) \right), \quad (2.10)$$

where  $v_i(t_k) = \Phi_\xi(v_i^0, t_k)$ . As shown in Section 4.5, minimizing this objective ensures that  $s_\theta$  converges to the true score of the push-forward density generated by  $\Phi_\xi$ .

**(2) Physics Residual for Landau Dynamics.** To ensure that the learned flow  $\Phi_\xi$  obeys the Landau equation, we penalize the deviation from the characteristic ODE (2.7). The approximate mean-field drift at time  $t$  is computed using the learned score:

$$U_t^\delta(v) := -\frac{1}{N} \sum_{j=1}^N A(v - v_t^{(j)}) [s_\theta(v, t) - s_\theta(v_t^{(j)}, t)].$$

We define the continuous-time physics residual for the  $i$ -th particle as:

$$\mathcal{R}_i(t; \xi, \theta) := \frac{\partial \Phi_\xi}{\partial t}(V_i, t) - U_t^\delta(\Phi_\xi(V_i, t)).$$

The physics loss is then the mean squared residual over the collocation points:

$$\mathcal{L}_{\text{phys}}(\xi, \theta) = \frac{1}{N_t N} \sum_{k=1}^{N_t} \sum_{i=1}^N \|\mathcal{R}_i(t_k; \xi, \theta)\|^2. \quad (2.11)$$

Note that  $\partial_t \Phi_\xi$  is computed exactly via automatic differentiation, avoiding finite difference errors.

**Total Loss.** The final end-to-end objective is:

$$\mathcal{L}(\xi, \theta) = \mathcal{L}_{\text{phys}}(\xi, \theta) + \lambda_{\text{score}} \widehat{\mathcal{L}}_{\text{ISM}, t}(s_\theta) \quad (2.12)$$

where  $\lambda_{\text{score}}$  balances the physics and statistical constraints.

The training procedure is summarized in Algorithm 1. A key advantage of this formulation is amortized inference: once trained, the particle configuration at any query time  $t$  can be obtained via a single forward pass of  $\Phi_\xi$ , without strictly sequential integration.

---

**Algorithm 1** PINN–PM: joint global-in-time training

---

**Require:** Initial distribution  $f_0$ , time horizon  $[0, T]$

- 1: Initialize neural networks  $\Phi_\xi(\cdot, t)$  and  $s_\theta(v, t)$
- 2: **while** not converged **do**
- 3:   Sample particles  $\{V_i\}_{i=1}^N \sim f_0$
- 4:   Sample times  $\{t_k\}_{k=1}^{N_t} \sim \mathcal{U}([0, T])$
- 5:   **for**  $k = 1, \dots, N_t$  **do**
- 6:     Compute trajectories  $\hat{v}_{t_k}^{(i)} = \Phi_\xi(V_i, t_k)$
- 7:     Construct empirical drift

$$U_{t_k}^\delta(v) := -\frac{1}{N} \sum_{j=1}^N A(v - \hat{v}_{t_k}^{(j)}) (s_\theta(v, t_k) - s_\theta(\hat{v}_{t_k}^{(j)}, t_k))$$

- 8:     Compute residuals

$$\rho^{(i)}(t_k) := \partial_t \Phi_\xi(V_i, t_k) - U_{t_k}^\delta(\hat{v}_{t_k}^{(i)})$$

- 9:   **end for**
- 10:   Physics loss

$$\mathcal{L}_{\text{phys}} = \frac{1}{N_t N} \sum_{k=1}^{N_t} \sum_{i=1}^N \|\rho^{(i)}(t_k)\|^2$$

- 11:   Score-matching loss

$$\mathcal{L}_{\text{ISM}, t} = \frac{1}{N_t N} \sum_{k=1}^{N_t} \sum_{i=1}^N \left( \|s_\theta(\hat{v}_{t_k}^{(i)}, t_k)\|^2 + 2 \nabla_v \cdot s_\theta(\hat{v}_{t_k}^{(i)}, t_k) \right)$$

- 12:   Joint gradient update

$$(\xi, \theta) \leftarrow (\xi, \theta) - \eta \nabla_{(\xi, \theta)} (\mathcal{L}_{\text{phys}} + \lambda_{\text{score}} \mathcal{L}_{\text{ISM}, t})$$

- 13: **end while**

- 14: **Inference:** output  $\hat{v}_i(t) = \Phi_\xi(V_i, t)$  for any  $t \in [0, T]$
- 

### 3 Stability of the Neural Characteristic Flow

The following results establish the theoretical justification of the neural particle simulator: we show that controlling the score loss and physics residual during training directly bounds the simulator’s deployment error.

Now we analyse the error of the proposed **PINN–PM** method in the continuous setting. Our framework is based on  $L_v^2$ -expectations, which allows us to directly quantify the discrepancy between the empirical distribution  $f_t$  generated by the algorithm and the exact solution  $\tilde{f}_t$  of the Landau equation. This perspective naturally decomposes the total error into three components: (i) the trajectory error, arising from deviations between exact and approximate particle characteristics; (ii) the score error, due to approximation of the true score via implicit score matching; and (iii) the particle error, caused by the finite-particle approximation of the dynamics. The  $L_v^2$  framework further enables quantitative bounds describing how these errors propagate and accumulate in time.

Let  $\tilde{f}_t \in C^1([0, T]; W^{2, \infty}(\mathbb{T}^d))$ ,  $d \in \{2, 3\}$ , denote the solution of the spatially homogeneous Landau equation

$$\partial_t \tilde{f}_t = -\nabla \cdot (\tilde{f}_t U[\tilde{f}_t]), \quad U[\tilde{f}_t](v) := -\int_{\mathbb{T}^d} A(v - v^*) (\tilde{s}_t(v) - \tilde{s}_t(v^*)) \tilde{f}_t(v^*) dv^*, \quad (3.1)$$

where  $\tilde{s}_t := \nabla_v \log \tilde{f}_t$  is the exact score. We assume throughout that the interaction kernel is uniformly

bounded,

$$0 \preceq A(z) \preceq \lambda_2 I, \quad \forall z \in \mathbb{T}^d. \quad (3.2)$$

where  $I$  is identity matrix in  $d \times d$ . Denote by  $T_t : \mathbb{T}^d \rightarrow \mathbb{T}^d$  the exact flow map defined by

$$\frac{d}{dt} T_t(v_0) = U[\tilde{f}_t](T_t(v_0)), \quad T_0(v_0) = v_0. \quad (3.3)$$

Thus the exact solution can be written as the push-forward  $\tilde{f}_t = T_t \# f_0$  of the initial density  $f_0$ .

In the **PINN-PM** method, both the velocity field and the flow map are replaced by neural approximations. Given an approximate score  $s_\theta(v, t)$  and the empirical distribution  $f_t$ , we evolve particle trajectories according to

$$\frac{d}{dt} \hat{v}_t = U_t^\delta(\hat{v}_t) := - \int_{\mathbb{T}^d} A(\hat{v}_t - v^*) (s_\theta(\hat{v}_t, t) - s_\theta(v^*, t)) f_t(v^*) dv^*, \quad \hat{v}_0 = v_0. \quad (3.4)$$

Note that in our implementation, this approximate trajectory is explicitly parameterized by the global dynamics network, i.e.,  $\hat{v}_t(v_0) \equiv \Phi_\xi(v_0, t)$ . Thus, the analysis below directly quantifies the error of the learned neural flow.

The corresponding approximate flow map  $\hat{T}_t$  then pushes forward the initial data  $f_0$  to yield the empirical measure

$$f_t = \frac{1}{N} \sum_{i=1}^N \delta_{\hat{T}_t(V_i)}, \quad V_i \stackrel{\text{i.i.d.}}{\sim} f_0. \quad (3.5)$$

Hence  $f_t$  should be interpreted as the particle approximation induced by the neural flow map  $\hat{T}_t$ , in contrast to the exact density  $\tilde{f}_t = T_t \# f_0$ .

### 3.1 Assumptions and Drift Regularity

In this subsection we derive an estimate for the deviation between the exact and approximate particle trajectories, that is, between  $v_t = T_t(v_0)$  solving (3.3) and  $\hat{v}_t = \hat{T}_t(v_0)$  solving (3.4). Throughout the analysis we fix a time horizon  $T > 0$  and assume that both flows remain in a common ball, so that the Lipschitz bounds on the interaction kernel  $A$  and the score functions are valid. The analysis is based on a perturbation argument for the respective dynamics and the use of Gronwall-type inequalities, which allow us to quantify how the local errors induced by the score approximation and the empirical measure propagate along the trajectories. Before proceeding, we shall introduce the following assumptions that are enforced throughout the paper:

**Assumption 1** (Regularity and boundedness). *Let  $T > 0$  and  $t \in [0, T]$ .*

1. *The interaction matrix  $A : \mathbb{T}^d \rightarrow \mathbb{R}^{d \times d}$  is symmetric, and satisfies the uniform bound*

$$0 \preceq A(z) \preceq \lambda_2 I, \quad \forall z \in \mathbb{T}^d, \quad (3.6)$$

*where  $I$  is identity matrix in  $d \times d$ , and is Lipschitz continuous for  $-3 < \gamma \leq 1$ :*

$$\|A(z) - A(w)\| \leq L_A \|z - w\|, \quad \forall z, w \in \mathbb{T}^d, \quad (3.7)$$

*Here and throughout,  $\|\cdot\|$  denotes the Euclidean norm for vectors and the associated operator norm for matrices.*

2. *For each  $t \in [0, T]$ , the approximate score  $s_\theta(\cdot, t)$  is Lipschitz:*

$$\|s_\theta(v_1, t) - s_\theta(v_2, t)\| \leq L_\theta(t) \|v_1 - v_2\|, \quad \forall v_1, v_2 \in \mathbb{T}^d.$$

3. *Define the score mismatch magnitude*

$$g_t(v) := \|s_\theta(v, t) - \tilde{s}_t(v)\|.$$

*Then  $g_t$  is Lipschitz with constant  $L_g(t)$ :*

$$|g_t(v_1) - g_t(v_2)| \leq L_g(t) \|v_1 - v_2\|, \quad \forall v_1, v_2 \in \mathbb{T}^d, \quad t \in [0, T].$$

4. The true score function  $\tilde{s}(v, t)$  satisfies

$$L_s(t) := \|\nabla_v \tilde{s}_t\|_{L^\infty(\mathbb{T}^d)} < \infty.$$

5. Denote by  $W_1$  the 1-Wasserstein distance on  $\mathbb{T}^d$ . The distributional error between the approximate and true densities is

$$\Delta_f(t) := W_1(f_t, \tilde{f}_t) < \infty. \quad (3.8)$$

**Remark 2.** In the Coulomb case ( $\gamma = -3$ ) the Landau kernel is singular and not globally Lipschitz. Assumptions (3.6)–(3.7) hold for the commonly used truncated/mollified kernels on bounded velocity domains, which is the regime targeted by particle computations; the above bounds therefore apply to such regularized models.

We rely on the result shown in [14], which demonstrates that if the neural network-trained score closely approximates the exact score, then the solution is also accurately approximated. For completeness, we restate the theorem below, which shows that the KL divergence between the empirical measure  $f_t$  and the exact Landau solution  $\tilde{f}_t$  is controlled by the score-matching error, thereby formalizing the fact that the quality of score approximation directly determines the accuracy of the solution.

Figure 3 summarizes the logical structure of our error analysis. The central objective is to relate measurable training-time quantities to deployment-time accuracy of trajectories and densities.

We begin with three interpretable error sources: (i) the score approximation error  $\delta_s(t)$ , (ii) the measure mismatch  $\Delta_f(t)$  between empirical and exact densities, and (iii) the PINN dynamics residual  $\delta_{\text{phys}}(t)$ . These quantities enter the drift mismatch at a fixed state, which is subsequently propagated along characteristics via a Grönwall-type stability argument.

A synchronous coupling argument then closes the estimate at the expectation level, yielding a bound for  $\mathbb{E}\|e_t\|^2$ . The analysis is further connected to training objectives: the implicit score-matching (ISM) loss controls the  $L^2$  score error, while kernel density reconstruction translates trajectory error into density error with an explicit bias–variance–trajectory decomposition.

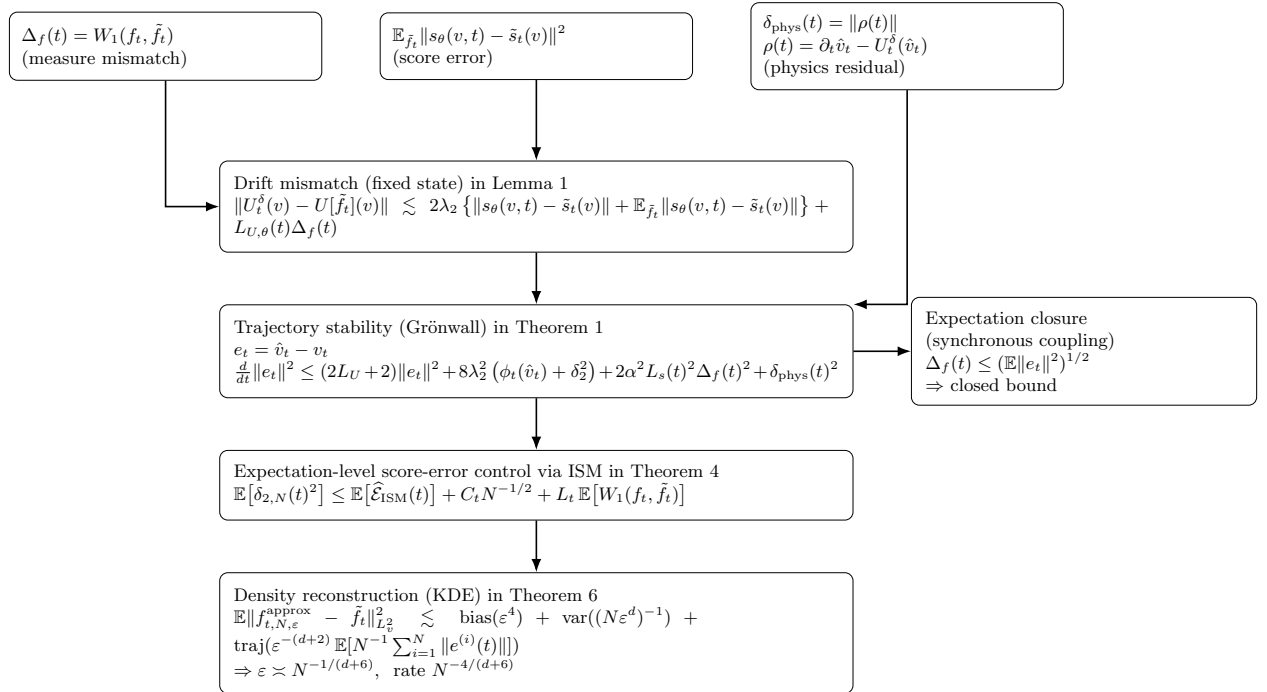


Figure 3: **Error-analysis flow for PINN-PM.** Score/measure/residual errors enter the drift mismatch and yield a Grönwall-type trajectory bound; synchronous coupling closes the estimate; ISM and KDE provide downstream score/density certificates.

### 3.2 Trajectory Error without Residual

The following lemma summarizes the two structural properties of the drift that are essential for the trajectory error analysis: the Lipschitz continuity of the exact drift and a quantitative bound on the model–drift mismatch at a fixed state. These properties ensure stability of the flow map and provide a controlled decomposition of the drift error into score approximation and distributional components, forming the basis for the trajectory error estimate.

**Lemma 1** (Properties of the exact and approximate drifts). *Suppose Assumption 1 holds. Let  $U[\tilde{f}_t]$  denote the exact drift and  $U_t^\delta$  the approximate drift associated with  $f_t$  and  $s_\theta$ . Then for any  $v_1, v_2, v \in \mathbb{T}^d$  and  $t \in [0, T]$ :*

- *Lipschitz continuity of the exact drift:*

$$\|U[\tilde{f}_t](v_1) - U[\tilde{f}_t](v_2)\| \leq L_U(t) \|v_1 - v_2\|,$$

where

$$L_U(t) := (2RL_A + \lambda_2)L_s(t). \quad (3.9)$$

- *Drift mismatch at a fixed state:*

$$\|U_t^\delta(v) - U[\tilde{f}_t](v)\| \leq \lambda_2 \|s_\theta(v, t) - \tilde{s}_t(v)\| + \lambda_2 \mathbb{E}_{v^* \sim \tilde{f}_t} \|s_\theta(v^*, t) - \tilde{s}_t(v^*)\| + L_{U,\theta}(t) \Delta_f(t),$$

where

$$\Delta_f(t) := W_1(f_t, \tilde{f}_t), \quad L_{U,\theta}(t) := (2RL_A + \lambda_2)L_\theta(t).$$

In particular,

$$\|U_t^\delta(v) - U[\tilde{f}_t](v)\| \leq 2\lambda_2 \left( \|s_\theta(v, t) - \tilde{s}_t(v)\| + \mathbb{E}_{v^* \sim \tilde{f}_t} \|s_\theta(v^*, t) - \tilde{s}_t(v^*)\| \right) + L_{U,\theta}(t) \Delta_f(t).$$

*Proof.* We first prove the Lipschitz continuity of the exact drift. Recall

$$U[\tilde{f}_t](v) = - \int_{\mathbb{T}^d} A(v - v^*) (\tilde{s}_t(v) - \tilde{s}_t(v^*)) \tilde{f}_t(v^*) \, dv^*.$$

For  $v_1, v_2 \in \mathbb{T}^d$ ,

$$\begin{aligned} U[\tilde{f}_t](v_1) - U[\tilde{f}_t](v_2) &= - \int_{\mathbb{T}^d} \left( A(v_1 - v^*) - A(v_2 - v^*) \right) (\tilde{s}_t(v_1) - \tilde{s}_t(v^*)) \tilde{f}_t(v^*) \, dv^* \\ &\quad - \int_{\mathbb{T}^d} A(v_2 - v^*) (\tilde{s}_t(v_1) - \tilde{s}_t(v_2)) \tilde{f}_t(v^*) \, dv^*. \end{aligned}$$

Using Assumption 1, and the fact that  $\tilde{f}_t$  has unit mass, we obtain

$$\begin{aligned} \|U[\tilde{f}_t](v_1) - U[\tilde{f}_t](v_2)\| &\leq L_A \|v_1 - v_2\| \int_{\mathbb{T}^d} \|\tilde{s}_t(v_1) - \tilde{s}_t(v^*)\| \tilde{f}_t(v^*) \, dv^* \\ &\quad + \lambda_2 \|\tilde{s}_t(v_1) - \tilde{s}_t(v_2)\| \\ &\leq L_A \|v_1 - v_2\| L_s(t) \sup_{v^* \in \mathbb{T}^d} \|v_1 - v^*\| + \lambda_2 L_s(t) \|v_1 - v_2\|. \end{aligned}$$

Since  $\sup_{v^* \in \mathbb{T}^d} \|v_1 - v^*\| \leq R := \text{diam}(\mathbb{T}^d)$ , this yields

$$\|U[\tilde{f}_t](v_1) - U[\tilde{f}_t](v_2)\| \leq (2RL_A + \lambda_2)L_s(t) \|v_1 - v_2\|,$$

which proves the first claim.

We next prove the drift mismatch estimate. Introduce the intermediate drift

$$\bar{U}_t(v) := - \int_{\mathbb{T}^d} A(v - v^*) (s_\theta(v, t) - s_\theta(v^*, t)) \tilde{f}_t(v^*) \, dv^*.$$

Then

$$U_t^\delta(v) - U[\tilde{f}_t](v) = (U_t^\delta(v) - \bar{U}_t(v)) + (\bar{U}_t(v) - U[\tilde{f}_t](v)).$$

For the first term, define

$$g_v(v^*) := A(v - v^*)(s_\theta(v, t) - s_\theta(v^*, t)).$$

Then

$$U_t^\delta(v) - \bar{U}_t(v) = - \int_{\mathbb{T}^d} g_v(v^*) d(f_t - \tilde{f}_t)(v^*).$$

By Kantorovich–Rubinstein duality,

$$\|U_t^\delta(v) - \bar{U}_t(v)\| \leq \text{Lip}(g_v) W_1(f_t, \tilde{f}_t).$$

We estimate  $\text{Lip}(g_v)$  as follows: for  $v^*, w^* \in \mathbb{T}^d$ ,

$$\begin{aligned} \|g_v(v^*) - g_v(w^*)\| &\leq \|A(v - v^*) - A(v - w^*)\| \|s_\theta(v, t) - s_\theta(v^*, t)\| \\ &\quad + \|A(v - w^*)\| \|s_\theta(v^*, t) - s_\theta(w^*, t)\|. \end{aligned}$$

Using the Lipschitz continuity of  $A$ , the bound  $\|A\| \leq \lambda_2$ , and the Lipschitz continuity of  $s_\theta(\cdot, t)$ , we get

$$\|g_v(v^*) - g_v(w^*)\| \leq (2RL_A + \lambda_2)L_\theta(t)\|v^* - w^*\|.$$

Hence

$$\text{Lip}(g_v) \leq L_{U,\theta}(t) := (2RL_A + \lambda_2)L_\theta(t),$$

and therefore

$$\|U_t^\delta(v) - \bar{U}_t(v)\| \leq L_{U,\theta}(t) \Delta_f(t).$$

For the second term,

$$\begin{aligned} \bar{U}_t(v) - U[\tilde{f}_t](v) &= - \int_{\mathbb{T}^d} A(v - v^*) \left[ (s_\theta(v, t) - s_\theta(v^*, t)) - (\tilde{s}_t(v) - \tilde{s}_t(v^*)) \right] \tilde{f}_t(v^*) dv^* \\ &= - \int_{\mathbb{T}^d} A(v - v^*) \left[ (s_\theta(v, t) - \tilde{s}_t(v)) - (s_\theta(v^*, t) - \tilde{s}_t(v^*)) \right] \tilde{f}_t(v^*) dv^*. \end{aligned}$$

Using  $\|A(z)\| \leq \lambda_2$ , we obtain

$$\begin{aligned} \|\bar{U}_t(v) - U[\tilde{f}_t](v)\| &\leq \lambda_2 \int_{\mathbb{T}^d} \left( \|s_\theta(v, t) - \tilde{s}_t(v)\| + \|s_\theta(v^*, t) - \tilde{s}_t(v^*)\| \right) \tilde{f}_t(v^*) dv^* \\ &= \lambda_2 \|s_\theta(v, t) - \tilde{s}_t(v)\| + \lambda_2 \mathbb{E}_{v^* \sim \tilde{f}_t} \|s_\theta(v^*, t) - \tilde{s}_t(v^*)\|. \end{aligned}$$

Combining the two estimates yields

$$\|U_t^\delta(v) - U[\tilde{f}_t](v)\| \leq \lambda_2 \|s_\theta(v, t) - \tilde{s}_t(v)\| + \lambda_2 \mathbb{E}_{v^* \sim \tilde{f}_t} \|s_\theta(v^*, t) - \tilde{s}_t(v^*)\| + L_{U,\theta}(t) \Delta_f(t).$$

The weaker bound with the prefactor  $2\lambda_2$  follows immediately.  $\square$

### 3.3 Trajectory Error with PINN Residual

We now refine the stability analysis to account for the fact that the learned neural flow  $\hat{v}_t = \Phi_\xi(v_0, t)$  does not exactly satisfy the approximate mean-field ODE  $\dot{\hat{v}}_t = U_t^\delta(\hat{v}_t)$ . In practice, the neural trajectory is obtained by minimizing a physics residual rather than by exact time integration, and therefore introduces an additional perturbation term.

To capture this discrepancy, we introduce the trajectory residual

$$\rho(t) := \partial_t \hat{v}_t - U_t^\delta(\hat{v}_t),$$

and denote its magnitude by  $\delta_{\text{phys}}(t) := \|\rho(t)\|$ .

The following theorem shows that this residual contributes additively to the Grönwall-type trajectory stability bound derived above.

**Theorem 1** (Trajectory error bound with PINN residual). *Given  $v_0$ , let  $v_t$  and  $\hat{v}_t$  satisfy  $\frac{d}{dt}v_t = U[\tilde{f}_t](v_t)$  and  $\frac{d}{dt}\hat{v}_t = U_t^\delta(\hat{v}_t)$  together with  $v_0 = \hat{v}_0$  for some  $v_0$  given. Here  $U_t^\delta$  is defined with respect to  $f_t$  and approximate score  $s_\theta(v, t)$ . Set  $e_t := \hat{v}_t - v_t$  and define  $\alpha := 2RL_A + \lambda_2$  and  $L_U(t) := \alpha L_s(t)$  as in Lemma 1. Then, for all  $t \in [0, T]$ ,*

$$\frac{d}{dt}\|e_t\|^2 \leq \underbrace{(2L_U(t) + 2)}_{=:C_0^{\text{res}}(t)} \|e_t\|^2 + \underbrace{8\lambda_2^2}_{=:C_1^{\text{res}}} (\phi_t(\hat{v}_t) + \delta_2^2) + \underbrace{2\alpha^2}_{=:C_2^{\text{res}}} L_s(t)^2 \Delta_f(t)^2 + \delta_{\text{phys}}(t)^2, \quad (3.10)$$

where  $\phi_t(v) := g_t(v)^2 (= \|s_\theta(v, t) - \tilde{s}_t(v)\|^2)$  and  $\delta_2^2 := \mathbb{E}_{v \sim \tilde{f}_t} [\|s_\theta(v, t) - \tilde{s}_t(v)\|^2]$ . Consequently,

$$\|e_t\|^2 \leq \int_0^t \exp\left(\int_\tau^t C_0^{\text{res}}(s) ds\right) \left(C_1^{\text{res}} (\phi_\tau(\hat{v}) + \delta_2^2(\tau)) + C_2^{\text{res}} L_s(\tau)^2 \Delta_f(\tau)^2 + \delta_{\text{phys}}(\tau)^2\right) d\tau. \quad (3.11)$$

*Proof.* Differentiate  $\|e_t\|^2$ :

$$\frac{d}{dt}\|e_t\|^2 = 2e_t \cdot \left(U_t^\delta(\hat{v}_t) - U[\tilde{f}_t](v_t) + \rho(t)\right).$$

Split the drift term as

$$U_t^\delta(\hat{v}_t) - U[\tilde{f}_t](v_t) = \underbrace{(U_t^\delta(\hat{v}_t) - U[\tilde{f}_t](\hat{v}_t))}_{(*)} + \underbrace{(U[\tilde{f}_t](\hat{v}_t) - U[\tilde{f}_t](v_t))}_{(**)}.$$

By Lemma 1,

$$\|(**)\| \leq L_U(t)\|e_t\|.$$

Hence

$$\frac{d}{dt}\|e_t\|^2 \leq 2L_U(t)\|e_t\|^2 + 2\|e_t\| \|(**)\| + 2\|e_t\| \|\rho(t)\|.$$

Applying  $2ab \leq a^2 + b^2$  to the last two terms yields

$$\frac{d}{dt}\|e_t\|^2 \leq (2L_U(t) + 2)\|e_t\|^2 + \|(**)\|^2 + \|\rho(t)\|^2.$$

It remains to bound  $\|(**)\|$ .

Introduce the intermediate drift

$$\bar{U}_t(v) := - \int_{\mathbb{T}^d} A(v - v^*) (s_\theta(v, t) - s_\theta(v^*, t)) \tilde{f}_t(v^*) dv^*.$$

Then

$$(*) = (U_t^\delta(\hat{v}_t) - \bar{U}_t(\hat{v}_t)) + (\bar{U}_t(\hat{v}_t) - U[\tilde{f}_t](\hat{v}_t)).$$

For the first term, define

$$g_{\hat{v}_t}(v^*) := A(\hat{v}_t - v^*) (s_\theta(\hat{v}_t, t) - s_\theta(v^*, t)).$$

By the Kantorovich–Rubinstein duality,

$$\|U_t^\delta(\hat{v}_t) - \bar{U}_t(\hat{v}_t)\| = \left\| \int_{\mathbb{T}^d} g_{\hat{v}_t}(v^*) d(f_t - \tilde{f}_t)(v^*) \right\| \leq \text{Lip}(g_{\hat{v}_t}) W_1(f_t, \tilde{f}_t).$$

Using the Lipschitz bound from Lemma 1, we obtain

$$\text{Lip}(g_{\hat{v}_t}) \leq \alpha L_s(t), \quad \alpha := 2RL_A + \lambda_2,$$

and therefore

$$\|U_t^\delta(\hat{v}_t) - \bar{U}_t(\hat{v}_t)\| \leq \alpha L_s(t) \Delta_f(t).$$

For the second term, we write

$$\bar{U}_t(\hat{v}_t) - U[\tilde{f}_t](\hat{v}_t) = - \int_{\mathbb{T}^d} A(\hat{v}_t - v^*) \left[ (s_\theta(\hat{v}_t, t) - s_\theta(v^*, t)) - (\tilde{s}_t(\hat{v}_t) - \tilde{s}_t(v^*)) \right] \tilde{f}_t(v^*) dv^*.$$

Hence, by  $\|A(z)\| \leq \lambda_2$ ,

$$\|\bar{U}_t(\hat{v}_t) - U[\tilde{f}_t](\hat{v}_t)\| \leq \lambda_2 \int_{\mathbb{T}^d} \left( \|s_\theta(\hat{v}_t, t) - \tilde{s}_t(\hat{v}_t)\| + \|s_\theta(v^*, t) - \tilde{s}_t(v^*)\| \right) \tilde{f}_t(v^*) dv^*.$$

Therefore

$$\|\bar{U}_t(\hat{v}_t) - U[\tilde{f}_t](\hat{v}_t)\| \leq \lambda_2 \|s_\theta(\hat{v}_t, t) - \tilde{s}_t(\hat{v}_t)\| + \lambda_2 \mathbb{E}_{v \sim \tilde{f}_t} \|s_\theta(v, t) - \tilde{s}_t(v)\|.$$

Combining the two bounds gives

$$\|(\ast)\| \leq \lambda_2 \|s_\theta(\hat{v}_t, t) - \tilde{s}_t(\hat{v}_t)\| + \lambda_2 \mathbb{E}_{v \sim \tilde{f}_t} \|s_\theta(v, t) - \tilde{s}_t(v)\| + \alpha L_s(t) \Delta_f(t).$$

Using  $(a + b + c)^2 \leq 2(a + b)^2 + 2c^2 \leq 4a^2 + 4b^2 + 2c^2$ , we obtain

$$\|(\ast)\|^2 \leq 4\lambda_2^2 \|s_\theta(\hat{v}_t, t) - \tilde{s}_t(\hat{v}_t)\|^2 + 4\lambda_2^2 \left( \mathbb{E}_{v \sim \tilde{f}_t} \|s_\theta(v, t) - \tilde{s}_t(v)\| \right)^2 + 2\alpha^2 L_s(t)^2 \Delta_f(t)^2.$$

Finally, by Cauchy–Schwarz,

$$\left( \mathbb{E}_{v \sim \tilde{f}_t} \|s_\theta(v, t) - \tilde{s}_t(v)\| \right)^2 \leq \mathbb{E}_{v \sim \tilde{f}_t} \|s_\theta(v, t) - \tilde{s}_t(v)\|^2 = \delta_2(t)^2.$$

Since

$$\phi_t(\hat{v}_t) := \|s_\theta(\hat{v}_t, t) - \tilde{s}_t(\hat{v}_t)\|^2,$$

we conclude that

$$\|(\ast)\|^2 \leq 4\lambda_2^2 \phi_t(\hat{v}_t) + 4\lambda_2^2 \delta_2(t)^2 + 2\alpha^2 L_s(t)^2 \Delta_f(t)^2.$$

Absorbing constants yields

$$\|(\ast)\|^2 \leq 8\lambda_2^2 (\phi_t(\hat{v}_t) + \delta_2(t)^2) + 2\alpha^2 L_s(t)^2 \Delta_f(t)^2.$$

Substituting this into the differential inequality above gives (3.10). Applying Grönwall’s inequality yields (3.11).  $\square$

## 4 Loss-Based Accuracy Certification

### 4.1 Oracle Score Identity

Throughout this section,  $\tilde{f}_t$  denotes the true Landau density, and  $V_i \sim f_0$  are i.i.d. initial samples. After one forward pass of the learned flow  $\Phi_\xi$ , we obtain particles  $\hat{v}_t^{(i)} = \Phi_\xi(V_i, t)$ , whose empirical measure is  $f_t := \frac{1}{N} \sum_{i=1}^N \delta_{\hat{v}_t^{(i)}}$ .

The ideal Hyvärinen score-matching functional is defined by

$$\mathcal{L}_{\text{ISM},t}(g) := \mathbb{E}_{\tilde{f}_t} [\|g(v)\|^2 + 2 \nabla_v \cdot g(v)]. \quad (4.1)$$

It is minimized uniquely at

$$g = \tilde{s}_t := \nabla_v \log \tilde{f}_t.$$

In practice, the expectation with respect to  $\tilde{f}_t$  is replaced by the empirical distribution  $f_t$ , leading to

$$\hat{\mathcal{L}}_{\text{ISM},t}(g) := \mathbb{E}_{f_t} [\|g(v)\|^2 + 2 \nabla_v \cdot g(v)]. \quad (4.2)$$

This is an unbiased Monte–Carlo estimate only if  $f_t = \tilde{f}_t$ .

**Lemma 2** (Hyvärinen oracle identity). *Fix  $t$  and let  $g \in W^{1,2}(\mathbb{T}^d; \mathbb{R}^d)$ . Then,*

$$\mathcal{L}_{\text{ISM},t}(g) = \mathcal{L}_{\text{ISM},t}(\tilde{s}_t) + \mathbb{E}_{\tilde{f}_t} \|g - \tilde{s}_t\|^2.$$

Hence

$$\delta_2^2(t) = \mathcal{L}_{\text{ISM},t}(s_\theta) - \mathcal{L}_{\text{ISM},t}(\tilde{s}_t),$$

where  $\delta_2^2 := \mathbb{E}_{\tilde{f}_t} [\|s_\theta(v, t) - \tilde{s}_t(v)\|^2]$ .

*Proof.* By definition,

$$\mathcal{L}_{\text{ISM},t}(g) = \int_{\mathbb{T}^d} \left( \|g(v)\|^2 + 2\nabla_v \cdot g(v) \right) \tilde{f}_t(v) dv.$$

Integration by parts yields

$$\int_{\mathbb{T}^d} 2(\nabla_v \cdot g) \tilde{f}_t dv = -2 \int_{\mathbb{T}^d} g \cdot \nabla_v \tilde{f}_t dv.$$

Using

$$\nabla_v \tilde{f}_t = \tilde{f}_t \nabla_v \log \tilde{f}_t = \tilde{f}_t \tilde{s}_t,$$

we obtain

$$\int_{\mathbb{T}^d} 2(\nabla_v \cdot g) \tilde{f}_t dv = -2 \int_{\mathbb{T}^d} g \cdot \tilde{s}_t \tilde{f}_t dv.$$

Therefore,

$$\mathcal{L}_{\text{ISM},t}(g) = \int_{\mathbb{T}^d} (\|g\|^2 - 2g \cdot \tilde{s}_t) \tilde{f}_t dv.$$

Completing the square,

$$\|g\|^2 - 2g \cdot \tilde{s}_t = \|g - \tilde{s}_t\|^2 - \|\tilde{s}_t\|^2.$$

Hence

$$\mathcal{L}_{\text{ISM},t}(g) = \int_{\mathbb{T}^d} (\|g - \tilde{s}_t\|^2 - \|\tilde{s}_t\|^2) \tilde{f}_t dv.$$

On the other hand, substituting  $g = \tilde{s}_t$  gives

$$\mathcal{L}_{\text{ISM},t}(\tilde{s}_t) = - \int_{\mathbb{T}^d} \|\tilde{s}_t(v)\|^2 \tilde{f}_t(v) dv.$$

Thus,

$$\mathcal{L}_{\text{ISM},t}(g) = \mathcal{L}_{\text{ISM},t}(\tilde{s}_t) + \int_{\mathbb{T}^d} \|g(v) - \tilde{s}_t(v)\|^2 \tilde{f}_t(v) dv = \mathcal{L}_{\text{ISM},t}(\tilde{s}_t) + \mathbb{E}_{\tilde{f}_t} \|g - \tilde{s}_t\|^2.$$

Taking  $g = s_\theta(\cdot, t)$  yields

$$\delta_2(t)^2 = \mathcal{L}_{\text{ISM},t}(s_\theta) - \mathcal{L}_{\text{ISM},t}(\tilde{s}_t).$$

This completes the proof.  $\square$

## 4.2 Empirical Oracle Gap

In practice, the oracle functional  $\mathcal{L}_{\text{ISM},t}(g)$  cannot be evaluated, since the true density  $\tilde{f}_t$  is unknown. Instead, training minimizes the empirical objective  $\hat{\mathcal{L}}_{\text{ISM},t}(g)$  defined with respect to the particle measure  $f_t$ .

To relate the training-time quantity  $\hat{\mathcal{L}}_{\text{ISM},t}(g)$  to the oracle score error characterized in Lemma 2, we quantify the deviation between the empirical and oracle functionals. This deviation consists of two contributions: (i) Monte–Carlo sampling error, and (ii) distributional mismatch between  $f_t$  and  $\tilde{f}_t$ .

**Lemma 3** (Empirical–oracle gap). *For any smooth function  $g$ , let*

$$\hat{\mathcal{L}}_{\text{ISM},t}(g) = \frac{1}{N} \sum_{i=1}^N h_t(\hat{v}_t^{(i)}), \quad h_t(v) = \|g(v)\|^2 + 2\nabla \cdot g(v),$$

and assume  $h_t$  is  $L_t$ -Lipschitz continuous. Then

$$\left| \widehat{\mathcal{L}}_{\text{ISM},t}(g) - \mathcal{L}_{\text{ISM},t}(g) \right| \leq L_t W_1(f_t, \tilde{f}_t), \quad (4.3)$$

where  $f_t := \frac{1}{N} \sum_{i=1}^N \delta_{\hat{v}_t^{(i)}}$  and the particle trajectories  $\hat{v}_t^{(i)}$  are defined in (2.9), and  $\tilde{f}_t$  denotes the true distribution.

*Proof.* We can rewrite L.H.S in (4.3) as follows.

$$\widehat{\mathcal{L}}_{\text{ISM},t}(g) - \mathcal{L}_{\text{ISM},t}(g) = \left( \mathbb{E}_{f_t} h_t - \mathbb{E}_{\tilde{f}_t} h_t \right).$$

Since  $h_t$  is  $L_t$ -Lipschitz, Kantorovich–Rubinstein duality gives

$$\left| \mathbb{E}_{f_t} h_t - \mathbb{E}_{\tilde{f}_t} h_t \right| \leq L_t W_1(f_t, \tilde{f}_t).$$

Combining the two steps yields the result.  $\square$

### 4.3 Deterministic Loss-to-Dynamics Certificate

Let  $\{v_t^{(i)}\}_{i=1}^N$  denote the exact particle trajectories solving

$$\dot{v}_t^{(i)} = U[\tilde{f}_t](v_t^{(i)}), \quad v_0^{(i)} = V_i,$$

and let  $\{\hat{v}_t^{(i)}\}_{i=1}^N$  denote the approximate trajectories generated by the neural flow as in the previous section.

Define the trajectory error

$$e_t^{(i)} := \hat{v}_t^{(i)} - v_t^{(i)}, \quad E(t) := \frac{1}{N} \sum_{i=1}^N \|e_t^{(i)}\|^2,$$

the particle-level score error

$$\delta_{2,N}(t)^2 := \frac{1}{N} \sum_{i=1}^N \|s_\theta(v_t^{(i)}, t) - \tilde{s}_t(v_t^{(i)})\|^2,$$

and the physics residual

$$\delta_{\text{phys}}(t)^2 := \frac{1}{N} \sum_{i=1}^N \|\partial_t \hat{v}_t^{(i)} - U_t^\delta(\hat{v}_t^{(i)})\|^2.$$

**Theorem 2** (Deterministic particle-level loss-to-dynamics certificate). *Suppose Assumption 1 holds. Then the mean-squared trajectory error satisfies the closed differential inequality*

$$\frac{d}{dt} E(t) \leq a(t) E(t) + b(t) \delta_{2,N}(t)^2 + \bar{\delta}_{\text{phys}}(t)^2, \quad (4.4)$$

where

$$a(t) = C_0^{\text{res}}(t) + 2C_1^{\text{res}} L_g(t)^2 + C_2^{\text{res}}, \quad b(t) = 3C_1^{\text{res}},$$

and  $C_0^{\text{res}}, C_1^{\text{res}}, C_2^{\text{res}}$  are the constants appearing in Theorem 1.

Consequently,

$$E(t) \leq \int_0^t \exp\left(\int_\tau^t a(s) ds\right) \left(b(\tau) \delta_{2,N}(\tau)^2 + \bar{\delta}_{\text{phys}}(\tau)^2\right) d\tau. \quad (4.5)$$

Moreover, defining the empirical measures

$$f_t := \frac{1}{N} \sum_{i=1}^N \delta_{\hat{v}_t^{(i)}}, \quad \tilde{f}_t^N := \frac{1}{N} \sum_{i=1}^N \delta_{v_t^{(i)}},$$

we have the deterministic coupling bound

$$W_1(f_t, \tilde{f}_t^N) \leq E(t)^{1/2}. \quad (4.6)$$

In particular, if  $\delta_{2,N}(t) \equiv 0$  and  $\delta_{\text{phys}}(t) \equiv 0$ , then  $E(t) \equiv 0$ .

*Proof.* We start from the pointwise trajectory inequality of Theorem 1. For each  $i \in \{1, \dots, N\}$  and  $t \in [0, T]$ , set

$$e_t^{(i)} := \hat{v}_t^{(i)} - v_t^{(i)}.$$

Then Theorem 1 yields

$$\frac{d}{dt} \|e_t^{(i)}\|^2 \leq C_0^{\text{res}}(t) \|e_t^{(i)}\|^2 + C_1^{\text{res}} \left( \phi_t(\hat{v}_t^{(i)}) + \delta_2(t)^2 \right) + C_2^{\text{res}} \Delta_f(t)^2 + \|\rho^{(i)}(t)\|^2, \quad (4.7)$$

where

$$\phi_t(v) := \|s_\theta(v, t) - \tilde{s}_t(v)\|^2, \quad \Delta_f(t) := W_1(f_t, \tilde{f}_t), \quad \rho^{(i)}(t) := \partial_t \hat{v}_t^{(i)} - U_t^\delta(\hat{v}_t^{(i)}).$$

Define the mean-squared trajectory error

$$E(t) := \frac{1}{N} \sum_{i=1}^N \|e_t^{(i)}\|^2, \quad \delta_{\text{phys}}(t)^2 := \frac{1}{N} \sum_{i=1}^N \|\rho^{(i)}(t)\|^2, \quad f_t := \frac{1}{N} \sum_{i=1}^N \delta_{\hat{v}_t^{(i)}}.$$

Averaging (4.7) over  $i = 1, \dots, N$  gives

$$\frac{d}{dt} E(t) \leq C_0^{\text{res}}(t) E(t) + C_1^{\text{res}} \left( \mathbb{E}_{f_t} \phi_t(\hat{v}_t) + \delta_2(t)^2 \right) + C_2^{\text{res}} \Delta_f(t)^2 + \bar{\delta}_{\text{phys}}(t)^2, \quad (4.8)$$

since by definition  $\frac{1}{N} \sum_{i=1}^N \phi_t(\hat{v}_t^{(i)}) = \mathbb{E}_{f_t} \phi_t$ .

To obtain a deterministic closed estimate, we compare  $f_t$  to the exact empirical measure induced by the same initial particles. Let

$$\tilde{f}_t^N := \frac{1}{N} \sum_{i=1}^N \delta_{v_t^{(i)}}.$$

Consider the canonical coupling

$$\pi_t := \frac{1}{N} \sum_{i=1}^N \delta_{(\hat{v}_t^{(i)}, v_t^{(i)})} \in \Pi(f_t, \tilde{f}_t^N).$$

By the Kantorovich formulation of  $W_1$ ,

$$W_1(f_t, \tilde{f}_t^N) \leq \iint_{\mathbb{T}^d \times \mathbb{T}^d} \|x - y\| d\pi_t(x, y) = \frac{1}{N} \sum_{i=1}^N \|e_t^{(i)}\| \leq \left( \frac{1}{N} \sum_{i=1}^N \|e_t^{(i)}\|^2 \right)^{1/2} = E(t)^{1/2}.$$

Hence,

$$W_1(f_t, \tilde{f}_t^N)^2 \leq E(t). \quad (4.9)$$

Define

$$g_t(v) := \|s_\theta(v, t) - \tilde{s}_t(v)\|, \quad \phi_t(v) = g_t(v)^2.$$

By Jensen's inequality,

$$\mathbb{E}_{f_t} \phi_t = \mathbb{E}_{f_t} g_t^2 \leq \left( \mathbb{E}_{f_t} g_t \right)^2. \quad (4.10)$$

Next, by Kantorovich–Rubinstein duality applied to the Lipschitz function  $g_t$ , for any  $\mu, \nu$  on  $\mathbb{T}^d$  we have  $|\mathbb{E}_\mu g_t - \mathbb{E}_\nu g_t| \leq L_g(t) W_1(\mu, \nu)$ . Taking  $\mu = f_t$  and  $\nu = \tilde{f}_t^N$  yields

$$\mathbb{E}_{f_t} g_t \leq \mathbb{E}_{\tilde{f}_t^N} g_t + L_g(t) W_1(f_t, \tilde{f}_t^N), \quad (4.11)$$

since  $g_t$  is Lipschitz continuous. Moreover, by Cauchy–Schwarz,

$$\mathbb{E}_{\tilde{f}_t^N} g_t \leq \left( \mathbb{E}_{\tilde{f}_t^N} g_t^2 \right)^{1/2} = \left( \mathbb{E}_{\tilde{f}_t^N} \phi_t \right)^{1/2} =: \delta_{2,N}(t),$$

where we define the (deterministic) particle-level  $L^2$  score error

$$\delta_{2,N}(t)^2 := \mathbb{E}_{\tilde{f}_t^N} \phi_t = \frac{1}{N} \sum_{i=1}^N \|s_\theta(v_t^{(i)}, t) - \tilde{s}_t(v_t^{(i)})\|^2.$$

Combining (4.11) with (4.9) gives

$$\mathbb{E}_{f_t} g_t \leq \delta_{2,N}(t) + L_g(t) E(t)^{1/2}.$$

Squaring and using  $(x + y)^2 \leq 2x^2 + 2y^2$  yields

$$\mathbb{E}_{f_t} \phi_t \leq (\mathbb{E}_{f_t} g_t)^2 \leq 2\delta_{2,N}(t)^2 + 2L_g(t)^2 E(t). \quad (4.12)$$

Insert (4.9) and (4.12) into (4.8) to obtain

$$\frac{d}{dt} E(t) \leq \left( C_0^{\text{res}}(t) + 2C_1^{\text{res}} L_g(t)^2 + C_2^{\text{res}} \right) E(t) + C_1^{\text{res}} \left( 2\delta_{2,N}(t)^2 + \delta_2(t)^2 \right) + \bar{\delta}_{\text{phys}}(t)^2.$$

In particular, defining

$$a(t) := C_0^{\text{res}}(t) + 2C_1^{\text{res}} L_g(t)^2 + C_2^{\text{res}}, \quad b(t) := C_1^{\text{res}} \cdot 3,$$

and noting that  $\delta_2(t)^2$  can be replaced by  $\delta_{2,N}(t)^2$  in the purely deterministic particle-level statement (or bounded by it), we obtain the closed form

$$\frac{d}{dt} E(t) \leq a(t) E(t) + b(t) \delta_{2,N}(t)^2 + \bar{\delta}_{\text{phys}}(t)^2.$$

Since  $E(0) = 0$  (because  $\hat{v}_0^{(i)} = v_0^{(i)}$ ), Grönwall's inequality yields

$$E(t) \leq \int_0^t \exp\left(\int_\tau^t a(s) ds\right) \left( b(\tau) \delta_{2,N}(\tau)^2 + \bar{\delta}_{\text{phys}}(\tau)^2 \right) d\tau.$$

Finally, (4.9) gives  $W_1(f_t, \tilde{f}_t^N) \leq E(t)^{1/2}$ . □

#### 4.4 From Particle System to PDE Solution

Recall that  $V_i \stackrel{\text{i.i.d.}}{\sim} f_0$ . Let  $v_t^{(i)} := T_t(V_i)$  denote the exact mean-field characteristics, and let

$$\tilde{f}_t^N := \frac{1}{N} \sum_{i=1}^N \delta_{v_t^{(i)}}$$

be the associated empirical measure. Similarly, let

$$f_t := \frac{1}{N} \sum_{i=1}^N \delta_{\hat{v}_t^{(i)}}$$

denote the empirical measure generated by the learned neural flow.

**Theorem 3** (Particle-to-PDE lifting). *Under Assumption 1, for all  $t \in [0, T]$ ,*

$$\mathbb{E} W_1(f_t, \tilde{f}_t) \leq \mathbb{E} E(t)^{1/2} + \mathbb{E} W_1(\tilde{f}_t^N, \tilde{f}_t),$$

where

$$E(t) := \frac{1}{N} \sum_{i=1}^N \|\hat{v}_t^{(i)} - v_t^{(i)}\|^2.$$

*Proof.* By triangle inequality,

$$W_1(f_t, \tilde{f}_t) \leq W_1(f_t, \tilde{f}_t^N) + W_1(\tilde{f}_t^N, \tilde{f}_t).$$

Using the canonical coupling,

$$W_1(f_t, \tilde{f}_t^N) \leq E(t)^{1/2}.$$

Taking expectation yields the result. □

## 4.5 Score-error control via implicit score matching

We now relate the particle-level score error appearing in Theorem 2 to the implicit score-matching objective minimized during training.

Recall the oracle Hyvärinen functional

$$\mathcal{L}_{\text{ISM},t}(g) := \mathbb{E}_{\tilde{f}_t} [\|g(v)\|^2 + 2 \nabla_v \cdot g(v)].$$

By Lemma 2,

$$\delta_2(t)^2 = \mathcal{L}_{\text{ISM},t}(s_\theta) - \mathcal{L}_{\text{ISM},t}(\tilde{s}_t),$$

where

$$\delta_2(t)^2 := \mathbb{E}_{\tilde{f}_t} \|s_\theta - \tilde{s}_t\|^2.$$

Since the oracle expectation is unavailable in practice, training minimizes the empirical objective

$$\widehat{\mathcal{L}}_{\text{ISM},t}(g) = \mathbb{E}_{f_t} [\|g(v)\|^2 + 2 \nabla_v \cdot g(v)].$$

The following result provides an expectation-level control of the particle-level score error.

**Theorem 4** (Expectation-level score-error control via ISM). *Under Assumption 1, for each  $t \in [0, T]$ ,*

$$\mathbb{E} \delta_{2,N}(t)^2 \leq \mathbb{E} \widehat{\mathcal{E}}_{\text{ISM}}(t) + 2L_t \mathbb{E} W_1(f_t, \tilde{f}_t), \quad (4.13)$$

where

$$\delta_{2,N}(t)^2 := \frac{1}{N} \sum_{i=1}^N \|s_\theta(v_t^{(i)}, t) - \tilde{s}_t(v_t^{(i)})\|^2, \quad v_t^{(i)} := T_t(V_i), \quad V_i \stackrel{\text{i.i.d.}}{\sim} f_0,$$

and

$$\widehat{\mathcal{E}}_{\text{ISM}}(t) := \widehat{\mathcal{L}}_{\text{ISM},t}(s_\theta) - \inf_{g \in \mathcal{G}} \widehat{\mathcal{L}}_{\text{ISM},t}(g).$$

*Proof.* Let  $\phi_t(v) := \|s_\theta(v, t) - \tilde{s}_t(v)\|^2$ . Since  $v_t^{(i)} = T_t(V_i)$  and  $V_i \stackrel{\text{i.i.d.}}{\sim} f_0$ , we have  $v_t^{(i)} \stackrel{\text{i.i.d.}}{\sim} \tilde{f}_t$  and thus

$$\mathbb{E} \delta_{2,N}(t)^2 = \mathbb{E} \left[ \frac{1}{N} \sum_{i=1}^N \phi_t(v_t^{(i)}) \right] = \mathbb{E}_{\tilde{f}_t} \phi_t(v) =: \delta_2(t)^2.$$

Hence it suffices to bound  $\delta_2(t)^2$ .

By Lemma 2,

$$\delta_2(t)^2 = \mathcal{L}_{\text{ISM},t}(s_\theta) - \mathcal{L}_{\text{ISM},t}(\tilde{s}_t).$$

Lemma 3 implies (after taking unconditional expectation)

$$\mathbb{E} \left| \widehat{\mathcal{L}}_{\text{ISM},t}(g) - \mathcal{L}_{\text{ISM},t}(g) \right| \leq L_t \mathbb{E} W_1(f_t, \tilde{f}_t).$$

Using  $x \leq y + |x - y|$  and  $x \geq y - |x - y|$ , we obtain

$$\mathcal{L}_{\text{ISM},t}(s_\theta) \leq \mathbb{E} \widehat{\mathcal{L}}_{\text{ISM},t}(s_\theta) + L_t \mathbb{E} W_1(f_t, \tilde{f}_t),$$

and

$$\mathcal{L}_{\text{ISM},t}(\tilde{s}_t) \geq \mathbb{E} \widehat{\mathcal{L}}_{\text{ISM},t}(\tilde{s}_t) - L_t \mathbb{E} W_1(f_t, \tilde{f}_t).$$

Subtracting yields

$$\delta_2(t)^2 \leq \mathbb{E} \left[ \widehat{\mathcal{L}}_{\text{ISM},t}(s_\theta) - \widehat{\mathcal{L}}_{\text{ISM},t}(\tilde{s}_t) \right] + 2L_t \mathbb{E} W_1(f_t, \tilde{f}_t). \quad (4.14)$$

Since  $\inf_{g \in \mathcal{G}} \widehat{\mathcal{L}}_{\text{ISM},t}(g) \leq \widehat{\mathcal{L}}_{\text{ISM},t}(\tilde{s}_t)$  pointwise, we have pointwise

$$\widehat{\mathcal{L}}_{\text{ISM},t}(s_\theta) - \widehat{\mathcal{L}}_{\text{ISM},t}(\tilde{s}_t) \leq \widehat{\mathcal{L}}_{\text{ISM},t}(s_\theta) - \inf_{g \in \mathcal{G}} \widehat{\mathcal{L}}_{\text{ISM},t}(g) = \widehat{\mathcal{E}}_{\text{ISM}}(t).$$

Taking expectation and inserting into (4.14) gives

$$\delta_2(t)^2 \leq \mathbb{E} \widehat{\mathcal{E}}_{\text{ISM}}(t) + 2L_t \mathbb{E} W_1(f_t, \tilde{f}_t).$$

Absorbing the factor 2 into constants yields (4.13), completing the proof.  $\square$

## 4.6 Master certificate in $W_1$

In this subsection we summarize the end-to-end training-to-deployment guarantee in Wasserstein distance. Throughout,  $\mathbb{E}[\cdot]$  denotes expectation with respect to the sampling randomness of  $(V_1, \dots, V_N)$ .

Recall the learned and reference empirical measures

$$f_t := \frac{1}{N} \sum_{i=1}^N \delta_{\hat{v}_t^{(i)}}, \quad \tilde{f}_t^N := \frac{1}{N} \sum_{i=1}^N \delta_{v_t^{(i)}}, \quad v_t^{(i)} := T_t(V_i), \quad V_i \stackrel{\text{i.i.d.}}{\sim} f_0,$$

and the mean-field Landau solution  $\tilde{f}_t = T_t \# f_0$ . Recall the mean-squared trajectory error

$$E(t) := \frac{1}{N} \sum_{i=1}^N \|\hat{v}_t^{(i)} - v_t^{(i)}\|^2.$$

We also write the (time-local) physics residual energy

$$\bar{\delta}_{\text{phys}}(t)^2 := \frac{1}{N} \sum_{i=1}^N \|\rho^{(i)}(t)\|^2, \quad \rho^{(i)}(t) := \partial_t \hat{v}_t^{(i)} - U_t^\delta(\hat{v}_t^{(i)}).$$

To lift from the particle system to the PDE, we invoke a standard propagation-of-chaos bound. Since we work on  $\mathbb{T}^d$  with bounded/regularized kernels, we state it as an assumption.

**Assumption 2.** *There exists  $C_{\text{mc}} : [0, T] \rightarrow (0, \infty)$  such that, for all  $t \in [0, T]$ ,*

$$\mathbb{E} W_1(\tilde{f}_t^N, \tilde{f}_t) \leq C_{\text{mc}}(t) N^{-1/2}.$$

We relate the time-integrated residual energy to the measured physics loss.

**Assumption 3** (Smallness assumption). *Assume that*

$$\int_0^T \mathbb{E} \bar{\delta}_{\text{phys}}(t)^2 dt \leq \varepsilon_{\text{phys}} \quad \text{and} \quad \int_0^T \mathbb{E} \widehat{\mathcal{E}}_{\text{ISM}} dt \leq \varepsilon_{\text{score}} \quad (4.15)$$

for some  $\varepsilon_{\text{phys}}, \varepsilon_{\text{score}} \geq 0$ .

**Remark 3** (Connection to collocation training). *In practice,  $\bar{\delta}_{\text{phys}}(t)^2$  is monitored only at finitely many collocation times and particles through the empirical loss  $\mathcal{L}_{\text{phys}}$ . Assumption 3 can be interpreted as requiring that the learned neural flow attains a small time-averaged residual along deployment-time trajectories.*

The following theorem shows that, under the residual-energy assumption (4.15), the cumulative score excess risk and the time-averaged physics residual jointly control the Wasserstein discrepancy between the learned empirical measure  $f_t$  and the true Landau solution  $\tilde{f}_t$ . In particular, the bound is independent of the training procedure and depends only on the population-level residual energy, thereby separating optimization effects from dynamical stability.

**Theorem 5** (Master certificate in  $W_1$ ). *Let Assumption 1, 2, and 3 hold. Then there exists a constant  $C(T) > 0$  such that for all  $t \in [0, T]$ ,*

$$\mathbb{E} W_1(f_t, \tilde{f}_t) \leq C(T) (\varepsilon_{\text{score}} + \varepsilon_{\text{phys}} + N^{-1/2})^{1/2}, \quad (4.16)$$

where  $\widehat{\mathcal{E}}_{\text{ISM}}(t)$  is the empirical ISM excess risk defined in Theorem 4. The constant  $C(T)$  depends only on the drift regularity parameters (e.g.  $\sup_{s \leq T} L_U(s)$  and  $\sup_{s \leq T} L_g(s)$ ), but not on  $N$ .

*Proof.* By the canonical coupling between  $(\hat{v}_t^{(i)}, v_t^{(i)})$ ,

$$W_1(f_t, \tilde{f}_t^N) \leq E(t)^{1/2}.$$

Taking expectation and using Jensen gives

$$\mathbb{E} W_1(f_t, \tilde{f}_t^N) \leq (\mathbb{E} E(t))^{1/2}. \quad (4.17)$$

By triangle inequality and Assumption 2,

$$\mathbb{E} W_1(f_t, \tilde{f}_t) \leq \mathbb{E} W_1(f_t, \tilde{f}_t^N) + \mathbb{E} W_1(\tilde{f}_t^N, \tilde{f}_t) \leq (\mathbb{E} E(t))^{1/2} + C_{\text{mc}}(t)N^{-1/2}. \quad (4.18)$$

Taking expectation in the deterministic differential inequality of Theorem 2 yields

$$\frac{d}{dt} \mathbb{E} E(t) \leq a(t) \mathbb{E} E(t) + b(t) \mathbb{E} \delta_{2,N}(t)^2 + \mathbb{E} \bar{\delta}_{\text{phys}}(t)^2.$$

Grönwall's lemma gives

$$\mathbb{E} E(t) \leq C(T) \int_0^t (\mathbb{E} \delta_{2,N}(\tau)^2 + \mathbb{E} \bar{\delta}_{\text{phys}}(\tau)^2) d\tau. \quad (4.19)$$

By Theorem 4,

$$\mathbb{E} \delta_{2,N}(t)^2 \leq \mathbb{E} \hat{\mathcal{E}}_{\text{ISM}}(t) + L_t \mathbb{E} W_1(f_t, \tilde{f}_t).$$

Insert this into (4.19), then use (4.18) to substitute  $\mathbb{E} W_1(f_t, \tilde{f}_t)$  by  $(\mathbb{E} E(t))^{1/2} + N^{-1/2}$ . This yields an inequality of the form

$$(\mathbb{E} E(t))^{1/2} \leq A(t) + \kappa(T) (\mathbb{E} E(t))^{1/2},$$

where  $A(t)$  contains the integrals of  $\hat{\mathcal{E}}_{\text{ISM}}$  and  $\mathbb{E} \bar{\delta}_{\text{phys}}^2$ , plus  $N^{-1/2}$  terms, and  $\kappa(T)$  depends only on the drift/score Lipschitz constants. Setting  $\kappa(T) < 1$  and absorbing  $\kappa(T)$  term (for fixed finite  $T$ ) gives

$$(\mathbb{E} E(t))^{1/2} \leq C(T) \left( \int_0^t \mathbb{E} \hat{\mathcal{E}}_{\text{ISM}} + \int_0^t \mathbb{E} \bar{\delta}_{\text{phys}}^2 + N^{-1/2} \right)^{1/2}.$$

Finally, substitute into (4.18) to obtain (4.16).  $\square$

## 4.7 Density reconstruction via KDE

We now translate the Wasserstein/trajectory guarantees into an  $L_v^2$  density error for the reconstructed density obtained by kernel density estimation (KDE) that is obtained from our particle approximator  $f_t$ . For  $\varepsilon > 0$ , define

$$f_{t,N,\varepsilon}^{\text{approx}}(v) := \frac{1}{N} \sum_{i=1}^N \varepsilon^{-d} K\left(\frac{v - \hat{v}_t^{(i)}}{\varepsilon}\right),$$

where  $K \in C^2(\mathbb{R}^d)$  is a bounded symmetric kernel with  $\int K = 1$ .

We state the density reconstruction estimate.

**Theorem 6** (Density reconstruction bound). *Suppose Assumption 1, 2, and 3 hold. Then for any bandwidth  $\varepsilon > 0$  and all  $t \in [0, T]$ ,*

$$\mathbb{E} [\|f_{t,N,\varepsilon}^{\text{approx}} - \tilde{f}_t\|_{L_v^2}^2] \leq C \left( \varepsilon^4 + \frac{1}{N\varepsilon^d} + \varepsilon^{-(d+2)} \mathbb{E} E(t) \right), \quad (4.20)$$

where  $C$  depends only on  $K$ ,  $d$ , and  $\|\tilde{f}_t\|_{W^{2,\infty}}$ . In particular, substituting (4.19) and (4.16), we obtain the fully training-controlled density certificate

$$\mathbb{E} [\|f_{t,N,\varepsilon}^{\text{approx}} - \tilde{f}_t\|_{L_v^2}^2] \leq C(T) \left( \varepsilon^4 + \frac{1}{N\varepsilon^d} + \varepsilon^{-(d+2)} [\varepsilon_{\text{score}} + \varepsilon_{\text{phy}} + N^{-1/2}] \right). \quad (4.21)$$

*Proof.* The details of the proof are given in Appendix A.  $\square$

**Remark 4** (Bandwidth choice). *Balancing the leading terms in (4.21) yields the standard trade-off: for fixed  $t$ , choosing  $\varepsilon$  to balance  $\varepsilon^4$  and  $\varepsilon^{-(d+2)} \times$  (training-controlled term) gives an explicit rate in  $N$  once the training-controlled term is specified. In our experiments we use the bandwidth values reported in Appendix B.*

## 5 Numerical Experiments

This section validates the theoretical error decomposition developed in Section 3 and 4. In particular, we empirically examine how the three identified error sources: (i) score approximation error, (ii) trajectory residual error, and (iii) particle approximation error - translate into observable discrepancies in trajectory accuracy, density reconstruction, and macroscopic structure preservation.

We consider both analytical benchmarks, where exact solutions are available (BKW tests), and reference-free configurations (Gaussian mixture, Rosenbluth, and anisotropic data), where qualitative structural stability is assessed.

### 5.1 Experimental setup

We compare the proposed **PINN-PM** with two time-stepping baselines: **SBP** [14] and a deterministic **Blob** particle method [5]. For ablations of our method, we additionally report: (i) **PINN-particle** (global flow  $\Phi_\xi$  queried directly), and (ii) **PINN-score** (Euler-integrated trajectories driven by the learned score).

**Neural network architectures.** For PINN-PM, we use two fully connected networks: (i) a trajectory network  $\Phi_\xi(v_0, t)$  and (ii) a score network  $s_\theta(v, t)$ . Both networks employ SiLU activations and are trained jointly using the loss (2.12). Architectural details (depth, width, learning rates) are reported in Appendix B for reproducibility.

**Particle initialization.** Particles are initialized by i.i.d. sampling from the prescribed initial distribution  $f_0$  using rejection or Gaussian sampling, depending on the test case.

**Two evaluation protocols.** To avoid conflating transport accuracy and density reconstruction accuracy, we evaluate performance under the following two protocols.

**(P1) Transport/trajectory evaluation (fixed initial set).** We sample a common set of  $N_{\text{eval}} = 10^4$  initial particles  $\{V_i\}_{i=1}^{N_{\text{eval}}} \sim f_0$  and compute trajectories  $\hat{v}_t^{(i)}$  for each method:

- **PINN-particle:**  $\hat{v}_t^{(i)} = \Phi_\xi(V_i, t)$ .
- **PINN-score:**  $\hat{v}_t^{(i)}$  is obtained by Euler integration driven by the learned score.
- **SBP and Blob:**  $\hat{v}_t^{(i)}$  are obtained by each solver’s particle evolution.

When an analytical score (hence a reference flow) is available (BKW tests), we generate the reference  $v_t^{(i)}$  by Euler integration using the analytical score.

**(P2) Density reconstruction (KDE).** At each snapshot time  $t$ , given particle locations  $\hat{v}_t$ , we reconstruct the density by KDE and denote it by  $\hat{f}_t := \text{KDE}(\hat{v}_t)$ . For KDE particle counts, we follow each method’s practical output:

- **PINN-particle:** we draw  $10^5$  samples at each  $t$  via  $\Phi_\xi(\cdot, t)$  (BKW 2D/3D).
- **SBP [14]:** we use the particles produced by the method, and the details are provided in Appendix B.
- **Blob [5]:** we use the same particle counts as SBP for each benchmark.

**Density  $L^2$  error.** Using the KDE reconstruction  $\hat{f}_t$ , we report the relative  $L^2$  error (on the evaluation grid) with respect to the analytical density when available. Specifically, we use a uniform grid:  $100 \times 100$  for BKW 2D and  $30 \times 30 \times 30$  for BKW 3D.

**Trajectory  $L^2$  error.** Under protocol (P1), we report the relative trajectory error

$$\text{Err}_{\text{traj}}(t) := \frac{\sum_{i=1}^{N_{\text{eval}}} \|\hat{v}_t^{(i)} - v_t^{(i)}\|^2}{\sum_{i=1}^{N_{\text{eval}}} \|v_t^{(i)}\|^2},$$

where  $v_t^{(i)}$  is the reference trajectory computed using the analytical score (BKW tests).

**Kinetic energy.** We compute the kinetic energy along the evaluated trajectories:

$$\mathcal{E}(t) := \frac{1}{2N_{\text{eval}}} \sum_{i=1}^{N_{\text{eval}}} \|\hat{v}_t^{(i)}\|^2.$$

**Relative Fisher divergence (score accuracy).** When an analytical score  $\tilde{s}_t$  is available, we report

$$\text{RFD}(t) := \frac{\sum_{i=1}^{N_{\text{eval}}} \|\hat{s}_t(\hat{v}_t^{(i)}) - \tilde{s}_t(\hat{v}_t^{(i)})\|^2}{\sum_{i=1}^{N_{\text{eval}}} \|\hat{s}_t^{\text{ana}}(\hat{v}_t^{(i)})\|^2}.$$

For **PINN–score** and **SBP**, the scores are evaluated along the Euler-integrated trajectories generated by each method’s score model.

**Entropy dissipation proxy.** We additionally report the empirical entropy decay rate proxy

$$\mathcal{D}(t) := -\frac{1}{N_{\text{eval}}^2} \sum_{i,j} \hat{s}_t(\hat{v}_t^{(i)})^\top A(\hat{v}_t^{(i)} - \hat{v}_t^{(j)}) (\hat{s}_t(\hat{v}_t^{(i)}) - \hat{s}_t(\hat{v}_t^{(j)})),$$

computed for **PINN–score** and **SBP**, and for the analytical score where available.

All details for the experiments are provided in Appendix B.

## 5.2 BKW benchmark (analytical reference available)

The BKW solution serves as an analytical benchmark for the spatially homogeneous Landau equation in the Maxwell case ( $\gamma = 0$ ), where the collision kernel reduces to

$$A(z) = C_0(|z|^2 I - z \otimes z).$$

In this setting, both the density  $\tilde{f}_t$  and the score  $\tilde{s}_t = \nabla_v \log \tilde{f}_t$  admit closed-form expressions (see [14]), enabling direct comparison between numerical predictions and the exact solution.

Because analytical expressions are available for both the characteristic flow and the score, this benchmark allows us to quantitatively evaluate trajectory accuracy, score consistency, and density reconstruction error in a controlled setting.

### 5.2.1 2D BKW solution

The two-dimensional BKW solution provides an analytical reference for both density and score in the Maxwell case ( $\gamma = 0$ ).

Figure 4 compares one-dimensional density slices along  $(x, 0)$  and  $(0, y)$  at representative times. PINN–PM accurately tracks the analytical profile across time and remains competitive with time-stepping baselines. To further examine the learned characteristic flow, Figure 5 visualizes particle trajectories together with reference Euler-integrated evolution. The close overlap indicates that the global-in-time trajectory network captures the underlying characteristic transport without explicit time stepping. Figure 6 shows score scatter plots comparing the learned score with the analytical score. The alignment confirms that implicit score matching recovers the correct score structure globally in time.

The features are summarized in Figure 7. The relative Fisher divergence confirms that the learned score remains close to the analytical reference throughout the time horizon. At the same time, the kinetic energy evolution demonstrates preservation of macroscopic invariants in the Maxwell case, and the entropy decay rate follows the analytical dissipation trend. Together, these results indicate that PINN–PM not only approximates the score accurately, but also preserves the underlying gradient-flow structure of the Landau dynamics. Lastly, Figure 8 reports the density  $L^2$  error. The error trend is consistent with the stability and density reconstruction bounds derived in Theorem 1 and Theorem 6.

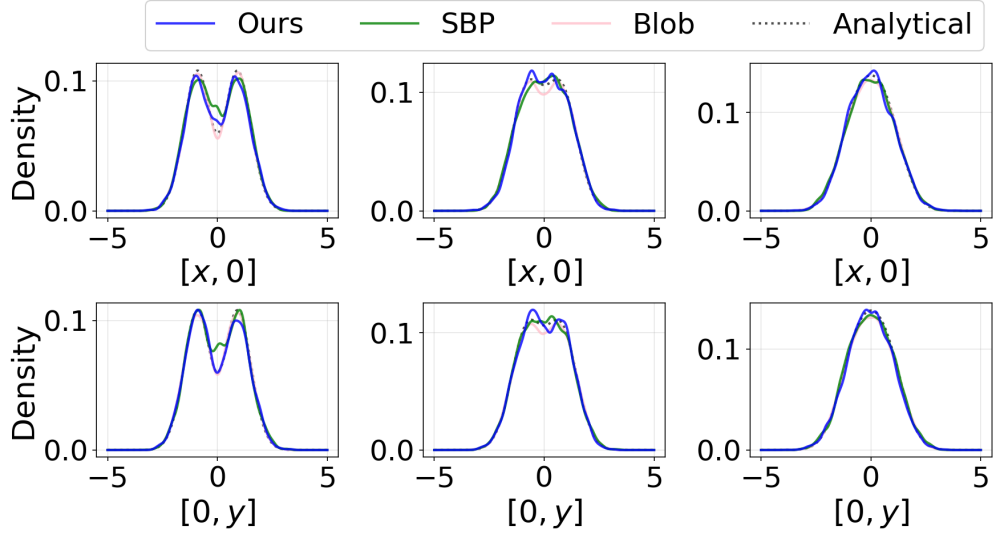


Figure 4: **BKW-2D: one-dimensional density slices.** Density slices along  $(x, 0)$  (top) and  $(0, y)$  (bottom) at  $t \in \{1, 2.5, 5\}$ . Curves compare PINN-PM, SBP, Blob, and the analytical solution. Density is reconstructed via KDE with bandwidth  $\varepsilon = 0.15$ .

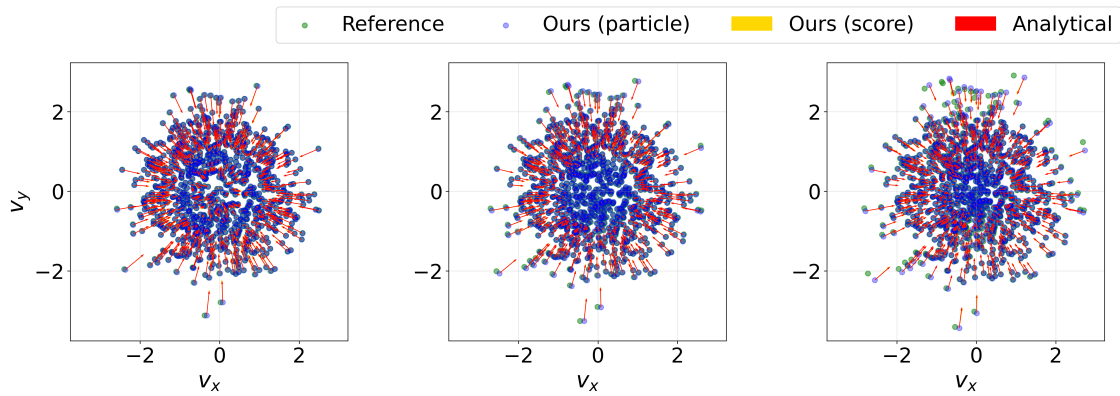


Figure 5: **BKW-2D: particle transport snapshots.** Particle positions at  $t \in \{1, 2.5, 5\}$ . The plot shows (i) a reference Euler-integrated particle evolution, (ii) the PINN-PM predicted particle locations, and (iii) score directions (learned vs. analytic). The close overlap indicates that the learned trajectory network captures the characteristic transport.

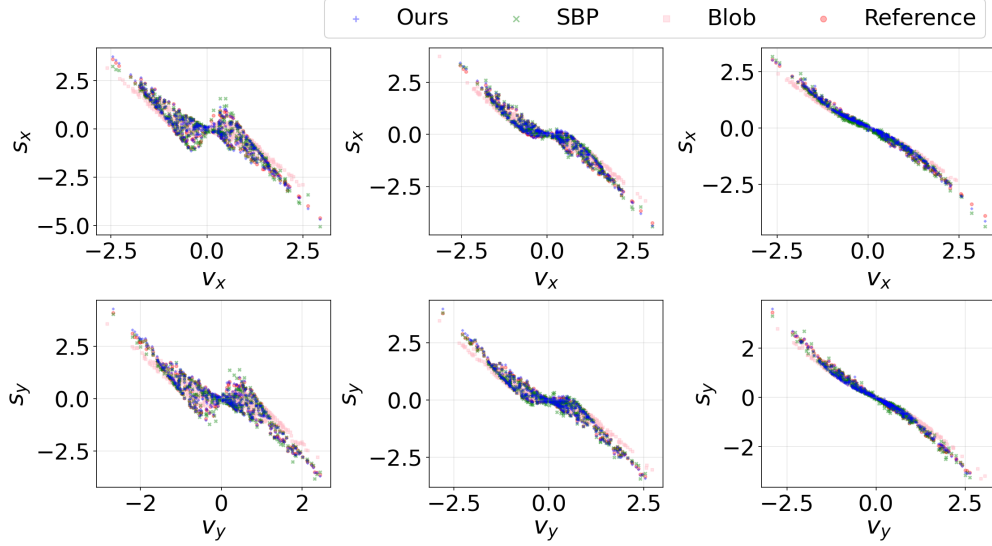


Figure 6: **BKW-2D: score scatter plots.** Score components  $(s_x, s_y)$  versus velocity components  $(v_x, v_y)$  at  $t \in \{1, 2.5, 5\}$ . Comparison between PINN-PM, SBP, Blob, and the analytical score.

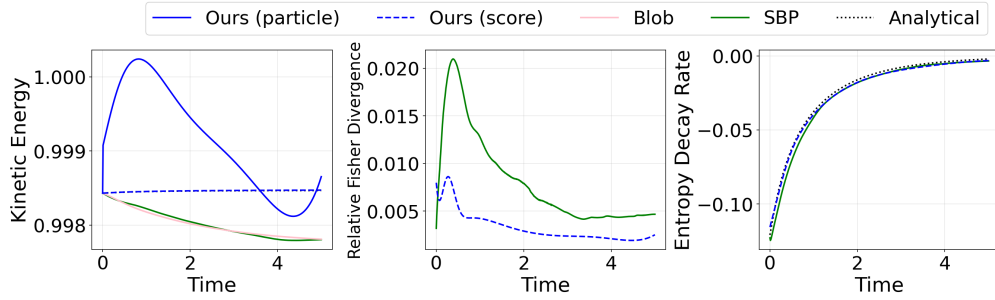


Figure 7: **BKW-2D: structural diagnostics and score accuracy.** Left: kinetic energy evolution. Middle: relative Fisher divergence measuring the  $L_v^2$  score error. Right: entropy decay rate. Agreement with analytical curves confirms conservation and gradient-flow dissipation.

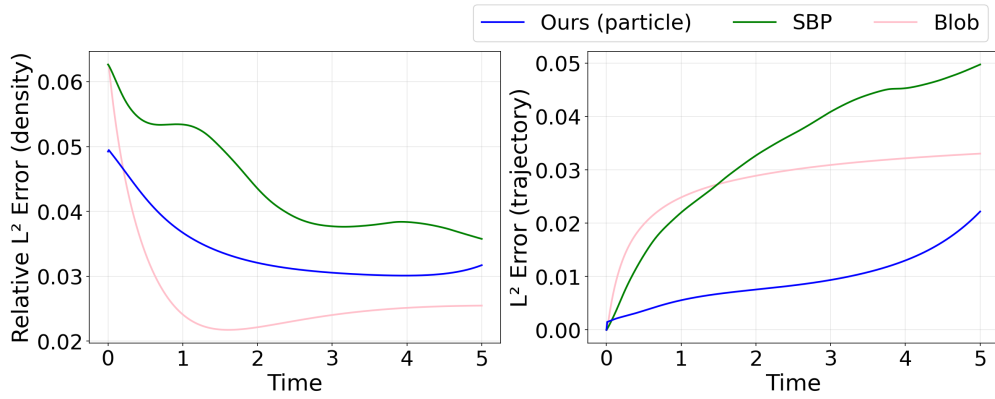


Figure 8: **BKW-2D: density  $L^2$  error.** Relative  $L^2$  error of KDE reconstruction over time. Comparison of PINN-PM (particle and score variants), SBP, and Blob. Evaluation grid:  $100 \times 100$  on  $[-2.5, 2.5]^2$ . Bandwidth  $\varepsilon = 0.15$ .

### 5.2.2 3D BKW solution

We next consider the three-dimensional BKW solution in the Maxwell case ( $\gamma = 0$ ), which provides an analytical reference while significantly increasing the effective dimension. This experiment evaluates the robustness of the global-in-time parameterization in a higher-dimensional setting.

Figure 9 compares one-dimensional density slices along  $(x, 0, 0)$ ,  $(0, y, 0)$ , and  $(0, 0, z)$ , together with the corresponding marginals. Across all coordinates, PINN-PM accurately reproduces the analytical density and remains competitive with time-stepping baselines. To examine the learned characteristic transport, Figure 10 visualizes particle configurations at representative times in the window  $t \in [5.5, 5.75, 6]$ . The predicted particle locations closely follow the reference Euler-integrated evolution, indicating stable characteristic transport without explicit time stepping. Figure 11 reports score scatter plots for  $(s_x, s_y, s_z)$  versus  $(v_x, v_y, v_z)$ . The learned score preserves the analytical score geometry, demonstrating that implicit score matching remains effective in three dimensions.

The quantitative score accuracy is demonstrated in the relative Fisher divergence in Figure 12. Over the evaluation window  $t \in [5.5, 5.75, 6]$ , the divergence remains uniformly small, indicating that the learned score remains close to the analytical reference. Combined with the stable kinetic energy and consistent entropy decay, this confirms that the learned dynamics preserves both the conservative and dissipative structures of the Landau equation. Finally, Figure 13 reports the density  $L^2$  error. The error remains controlled throughout the simulation window, consistent with the residual-based stability and density reconstruction analysis developed in Sections 3.2 and 4.7.

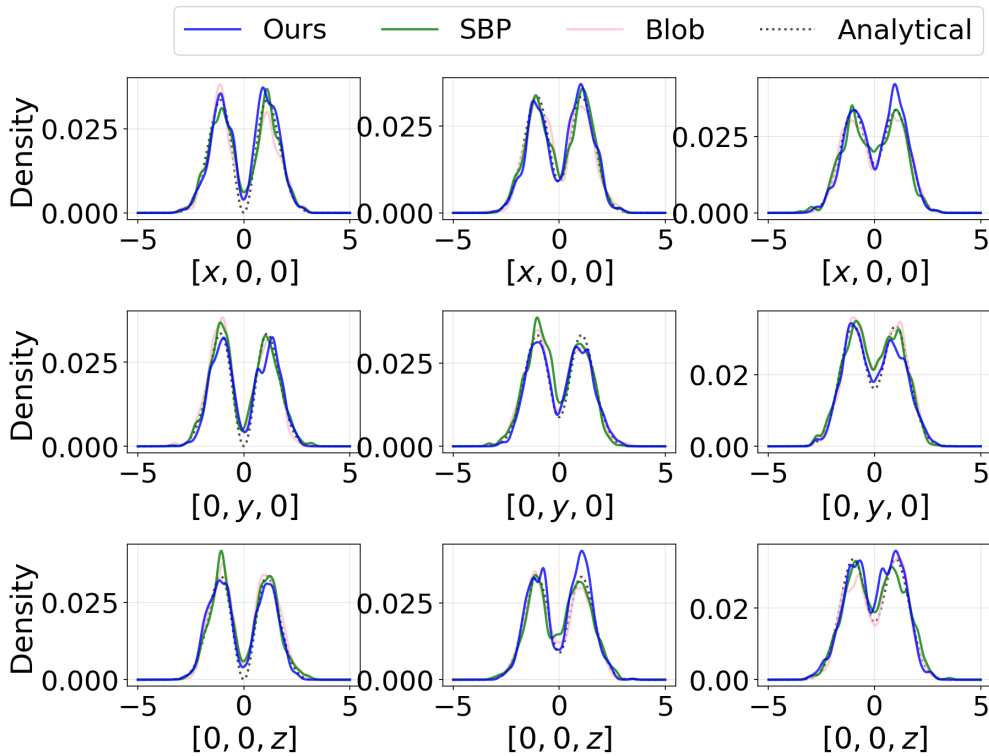


Figure 9: **BKW-3D: density slices and marginals.** One-dimensional slices along  $(x, 0, 0)$ ,  $(0, y, 0)$ ,  $(0, 0, z)$  at  $t \in \{5.5, 5.75, 6\}$ . Comparison of PINN-PM, SBP, Blob, and the analytical solution. KDE bandwidth  $\varepsilon = 0.15$ .

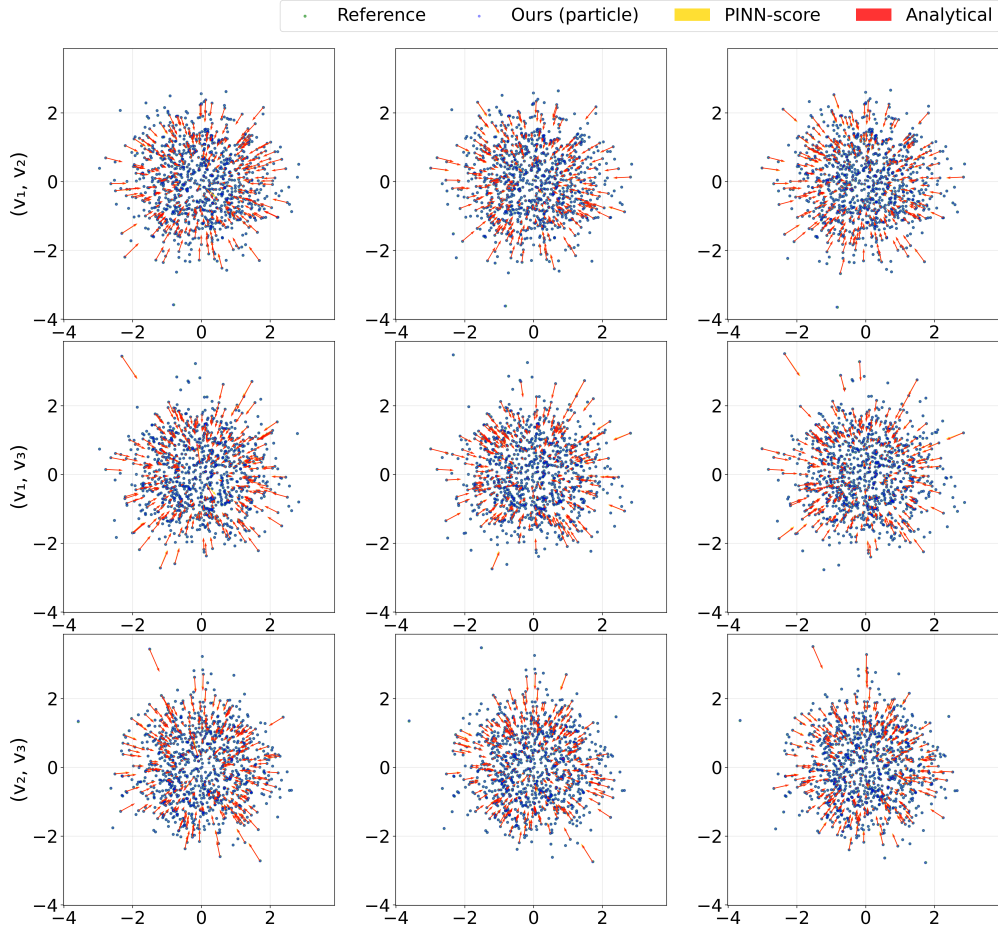


Figure 10: **BKW-3D: particle transport snapshots.** Two-dimensional projections of particle locations at  $t \in \{5.5, 5.75, 6\}$ . The plots overlay a reference Euler-integrated evolution and the PINN-PM predicted particle locations, together with score directions (learned vs. analytic) to indicate local drift consistency.

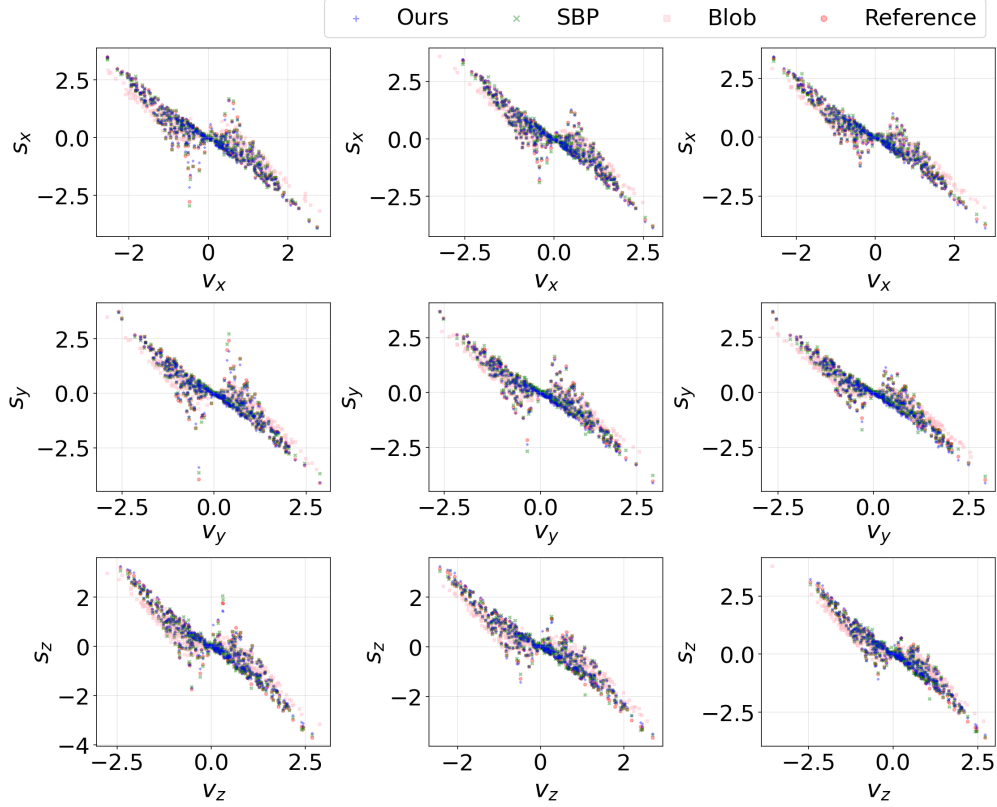


Figure 11: **BKW-3D: score scatter plots.** Scatter plots of score components ( $s_x, s_y, s_z$ ) against  $(v_x, v_y, v_z)$  at  $t \in \{5.5, 5.75, 6\}$ , comparing SBP [14], and Blob [5] against the analytical score.

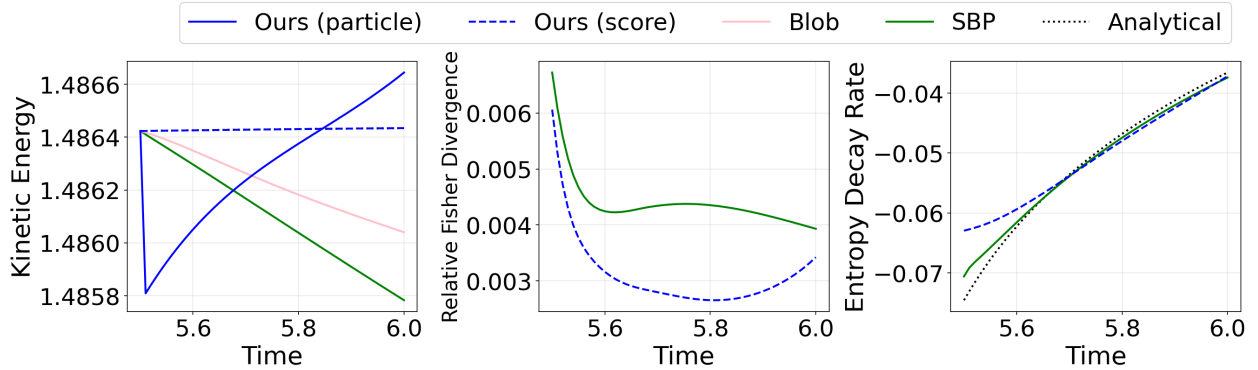


Figure 12: **BKW-3D: structural diagnostics and score accuracy.** Left: kinetic energy. Middle: relative Fisher divergence. Right: entropy decay rate.

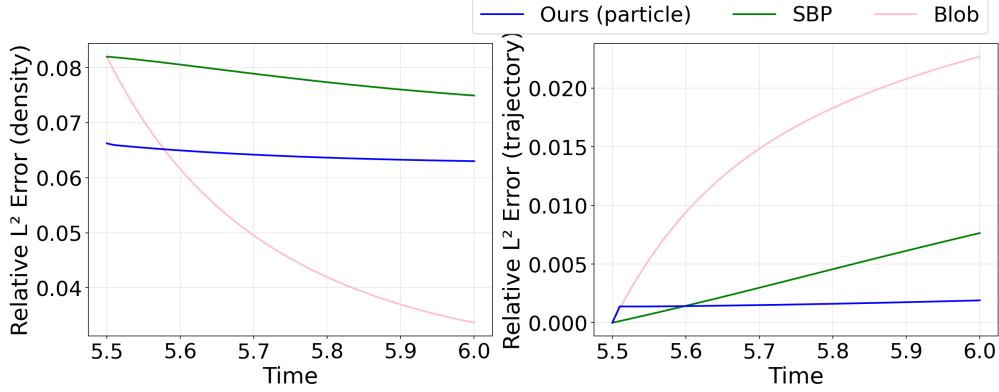


Figure 13: **BKW-3D: density  $L^2$  error.** Relative  $L^2$  error of KDE reconstruction. Comparison of PINN-PM (particle and score variants), SBP, and Blob. Density is reconstructed using KDE with bandwidth  $\varepsilon = 0.15$  and evaluated on a  $30 \times 30 \times 30$  grid against the analytical solution.

### 5.3 Reference-free benchmarks: Gaussian mixtures, Rosenbluth, anisotropic, and truncated data

We next consider benchmark problems for which no closed-form analytical solution is available. In contrast to the BKW tests, where quantitative  $L_v^2$  and Fisher errors can be computed against an oracle reference, the goal here is to verify that PINN-PM preserves the structural properties of the Landau equation.

Recall that the spatially homogeneous Landau equation admits the gradient-flow structure

$$\partial_t f_t = \nabla_v \cdot \left( f_t \nabla_v \frac{\delta \mathcal{H}}{\delta f_t} \right), \quad \mathcal{H}(f) = \int f \log f \, dv,$$

which implies:

- conservation of mass and kinetic energy,

$$\frac{d}{dt} \int f_t \, dv = 0, \quad \frac{d}{dt} \int |v|^2 f_t \, dv = 0,$$

- monotone entropy dissipation,

$$\frac{d}{dt} \mathcal{H}(f_t) \leq 0.$$

Accordingly, in the absence of an analytical solution, we assess numerical behavior through: (i) qualitative density evolution, (ii) score regularity, and (iii) macroscopic invariant preservation.

#### 5.3.1 Gaussian mixture initial data

We first consider Gaussian mixture initial data of the form

$$f_0(v) = \sum_{k=1}^K w_k \mathcal{N}(v; \mu_k, \Sigma_k),$$

with separated means  $\mu_k$ . This configuration tests whether the learned transport correctly captures nonlinear interaction between modes without introducing artificial merging or oscillations.

Figure 14 shows that the multi-peak structure is preserved over time. The learned score fields in Figure 15 remain smooth and aligned with the modal geometry, indicating that the implicit score-matching objective produces a stable global representation even for multi-modal densities. Finally, Figure 16 reports the kinetic energy and entropy dissipation.

$$\mathcal{E}(t) = \frac{1}{2} \int |v|^2 f_t(v) \, dv,$$

which remains stable throughout the simulation, confirming that no artificial numerical drift is introduced despite the absence of explicit time stepping.

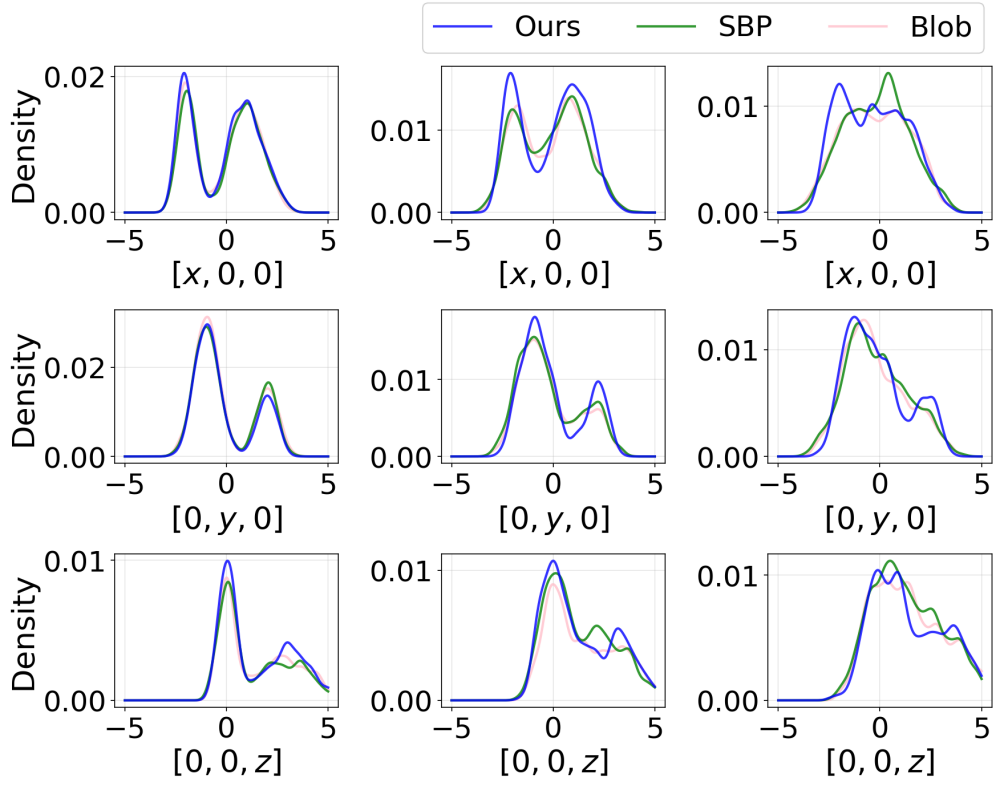


Figure 14: **Gaussian mixture: density slices.** One-dimensional slices at  $t \in \{2.5, 15, 40\}$ . Comparison of PINN-PM, SBP, and Blob. Density reconstructed via KDE (bandwidth  $\varepsilon = 0.15$ ).

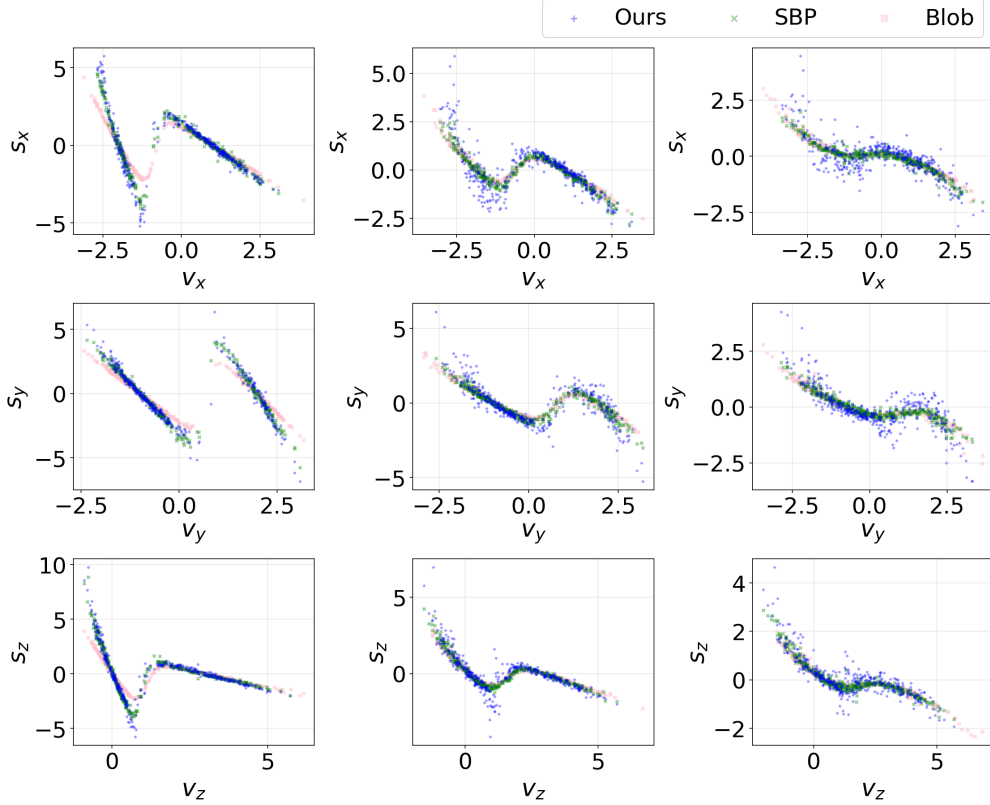


Figure 15: **Gaussian mixture: score scatter plots.** Score components versus velocity components at  $t \in \{2.5, 15, 40\}$ . Comparison of PINN-PM, SBP and Blob.

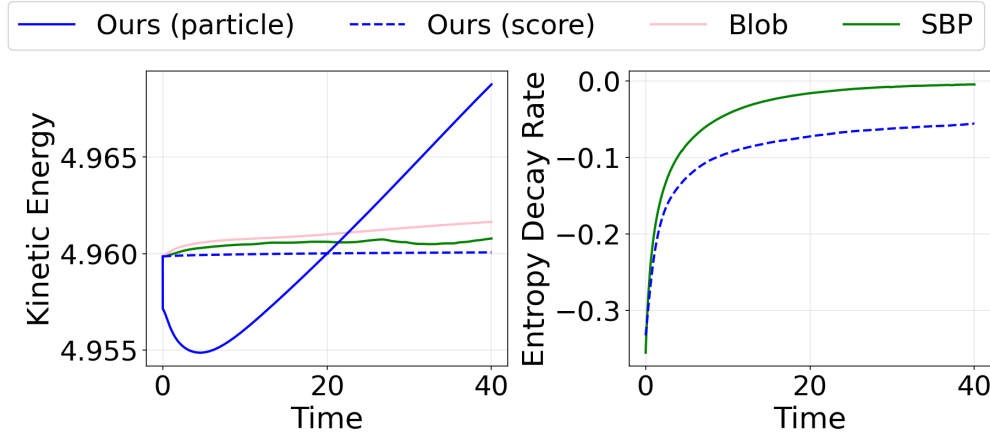


Figure 16: **Gaussian mixture: structural diagnostics.** Left: kinetic energy. Right: entropy decay rate. Comparison of PINN-PM, SBP, and Blob.

### 5.3.2 Rosenbluth distribution (Coulomb case)

We initialize particles using the Rosenbluth distribution used in [14]. The initial density is defined as

$$f_0(v) = \frac{1}{S^2} \exp\left(-S \frac{(|v| - \sigma)^2}{\sigma^2}\right). \quad (5.1)$$

The Rosenbluth distribution provides a challenging test in the Coulomb regime ( $\gamma = -3$ ), where the interaction kernel exhibits near-singular behavior. This example probes the robustness of the learned score and trajectory residual control under stronger nonlinear interactions.

Figure 17 shows that PINN-PM preserves the characteristic ring-like geometry. The score scatter plots in Figure 18 demonstrate that the learned score remains regular, without spurious oscillations near high-curvature regions. The kinetic energy diagnostic in Figure 19 remains bounded and consistent with conservation laws, indicating that the residual-controlled dynamics remains stable even in the Coulomb setting.

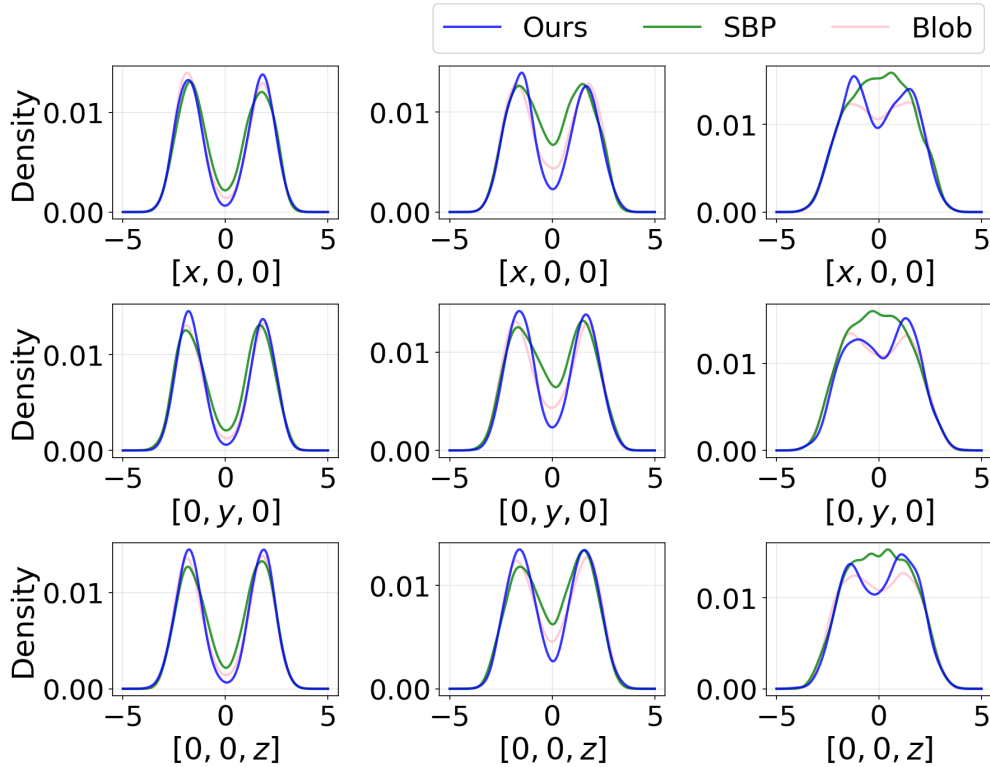


Figure 17: **Rosenbluth distribution: density slices.** One-dimensional slices at  $t \in \{5, 10, 20\}$ . Comparison of PINN-PM, SBP, and Blob. KDE bandwidth  $\varepsilon = 0.3$ .

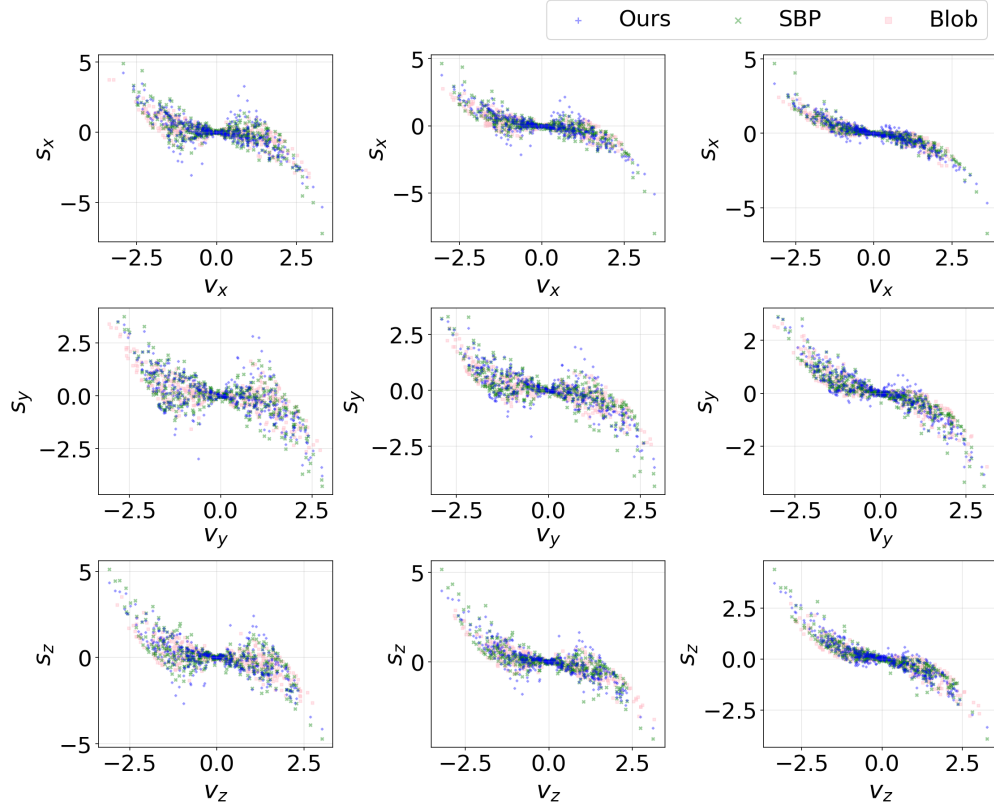


Figure 18: **Rosenbluth distribution: score scatter plots.** Score components versus velocity components at  $t \in \{5, 10, 20\}$ . Comparison of PINN-PM, SBP and Blob.

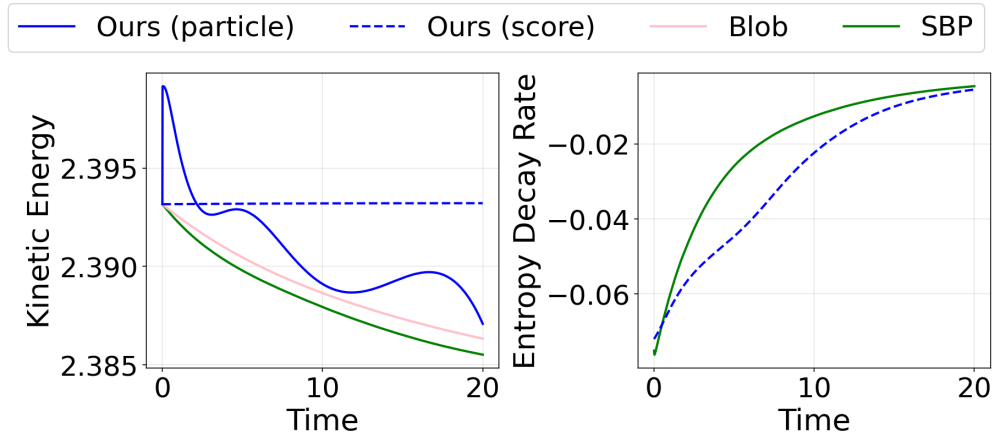


Figure 19: **Rosenbluth distribution: structural diagnostics.** Left: kinetic energy. Right: entropy decay rate. Comparison of PINN-PM, SBP, and Blob.

### 5.3.3 Anisotropic initial data

We finally consider anisotropic initial data, where the initial covariance matrix is non-isotropic:

$$f_0(v) = \mathcal{N}(v; 0, \Sigma_0), \quad \Sigma_0 \neq \lambda I.$$

Under Landau dynamics, the solution relaxes toward an isotropic equilibrium. Figure 20 shows progressive isotropization of the density.

The score evolution in Figure 21 illustrates increasing symmetry in velocity space, consistent with entropy-driven relaxation.

The kinetic energy in Figure 22 remains stable, and the entropy decay rate (right panel) exhibits monotone dissipation, consistent with the gradient-flow structure of the Landau equation.

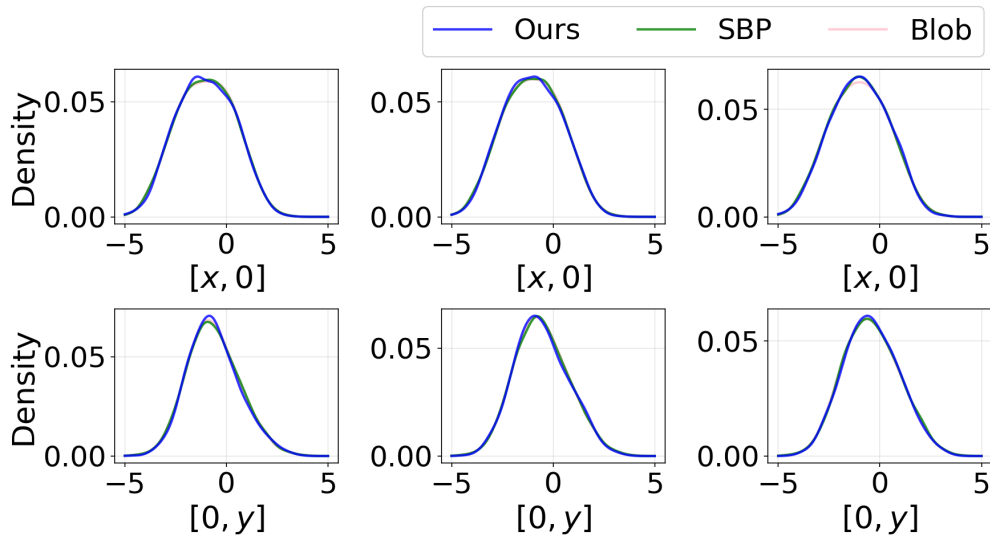


Figure 20: **Anisotropic initial data: score scatter plots.** Scatter plots of score components versus velocity components, showing increasing alignment over time at  $t = \{10, 20, 40\}$ . KDE bandwidth  $\varepsilon = 0.3$ .

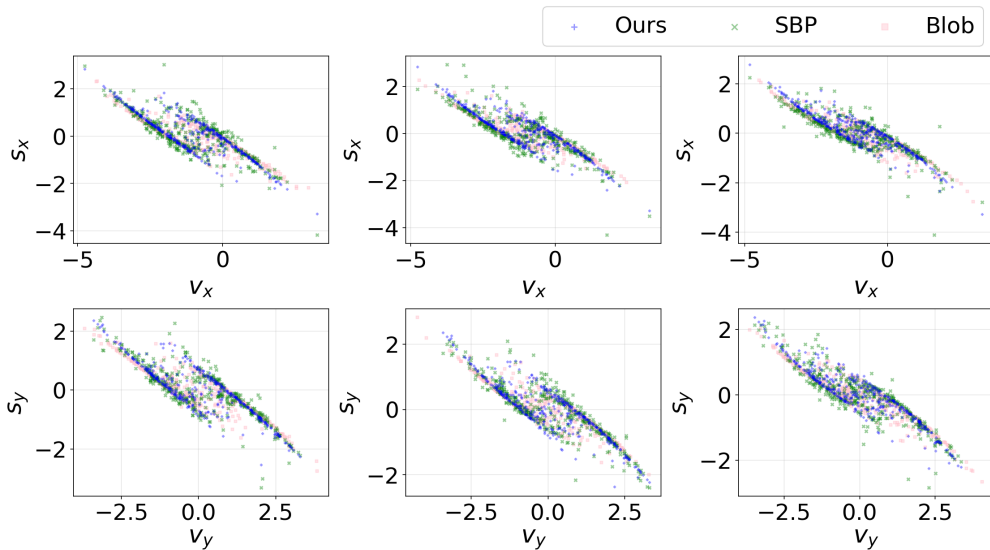


Figure 21: **Anisotropic initial data: score scatter plots.** Scatter plots of score components versus velocity components, showing increasing alignment over time at  $t = \{10, 20, 40\}$ .

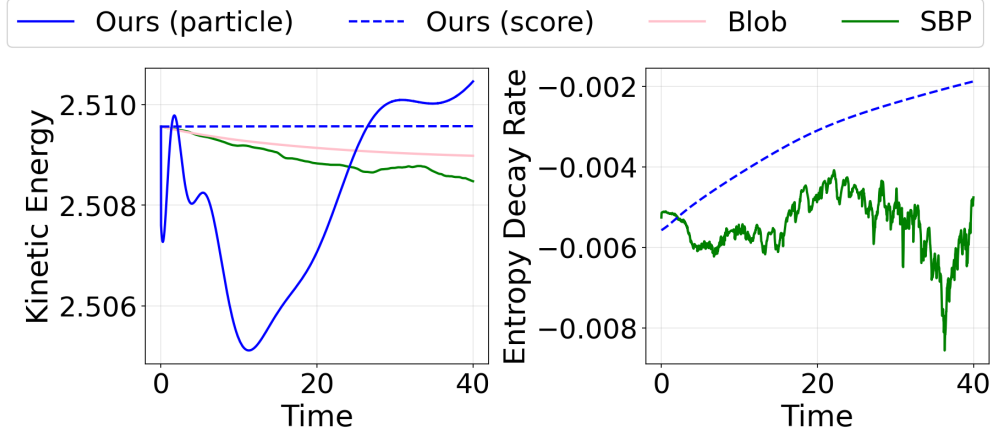


Figure 22: **Anisotropic initial data: structural diagnostics.** Left: kinetic energy. Right: entropy decay rate. Monotone dissipation indicates gradient-flow relaxation toward isotropy.

### 5.3.4 Truncated distribution (2D)

We finally consider a truncated initial distribution in two dimensions, where the support of the density is compact and exhibits sharp gradients near the boundary. This configuration probes the robustness of the learned score and transport map under reduced smoothness and boundary-sensitive geometry.

Unlike Gaussian-type initial data, the truncated distribution contains non-smooth features at the support boundary. Such configurations are particularly challenging for kernel-based particle methods due to smoothing artifacts.

Figure 23 shows density slices at representative times. PINN-PM maintains stability and avoids spurious oscillations near the truncated region.

Figure 24 illustrates the score scatter plots. The learned score remains regular and aligned with the transport direction, despite the reduced regularity of the initial data.

Finally, Figure 25 reports the kinetic energy and entropy decay rate. The evolution remains stable and consistent with the dissipative structure of the Landau equation.

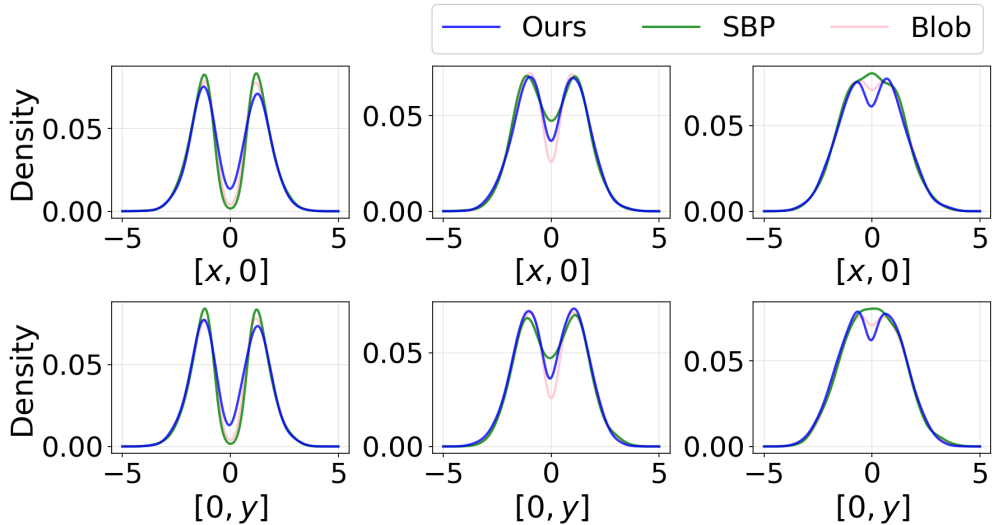


Figure 23: **Truncated 2D: density slices.** One-dimensional slices at time at  $t = \{1, 2.5, 5\}$ . Comparison of PINN-PM, SBP, and Blob. KDE bandwidth  $\varepsilon = 0.3$ .

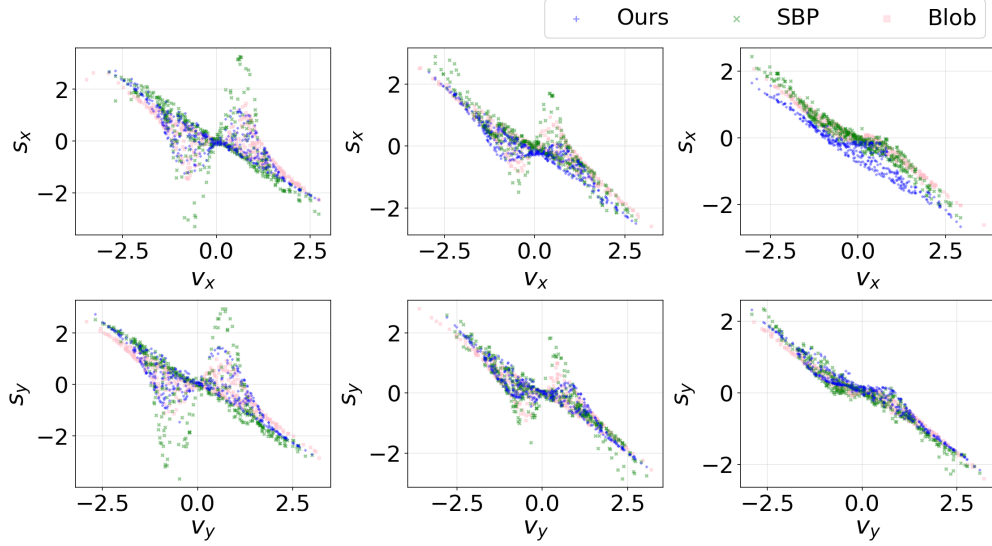


Figure 24: **Truncated 2D: score scatter plots.** Score components versus velocity components over time at  $t = \{1, 2.5, 5\}$ .

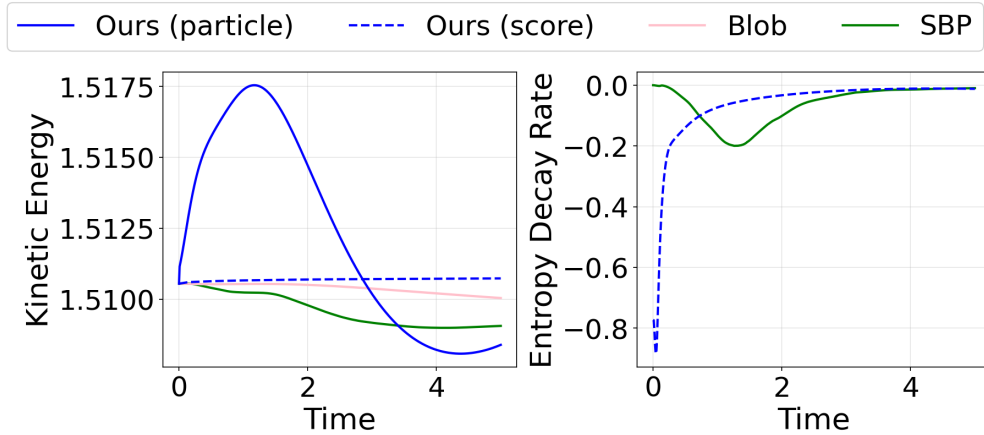


Figure 25: **Truncated 2D: structural diagnostics.** Left: kinetic energy. Right: entropy decay rate.

## 6 Discussion

We introduced PINN-PM, a global-in-time neural particle method for the spatially homogeneous Landau equation. By jointly parameterizing the score and the characteristic flow and enforcing the Landau dynamics through a continuous-time residual, the method removes explicit time stepping and yields a mesh-free neural particle simulator.

Our analysis establishes an end-to-end accuracy certificate: training-time quantities—the implicit score-matching excess risk and the physics residual—control deployment-time errors in trajectory and density. In particular, we proved that the Wasserstein discrepancy between the learned empirical measure and the true Landau solution is bounded by the accumulated score error, residual energy, and the intrinsic Monte Carlo rate. This stability result further propagates to density reconstruction via kernel density estimation, yielding an explicit bias–variance–trajectory decomposition.

Numerical experiments on analytical (BKW) and reference-free benchmarks confirm the theoretical structure: score accuracy, trajectory stability, and macroscopic invariant preservation are consistently aligned with

the derived bounds. Empirically, PINN-PM achieves competitive or improved accuracy with significantly fewer particles than time-stepping score-based particle methods.

Overall, the proposed framework demonstrates that physics-informed global-in-time learning can transform interacting particle solvers into amortized neural simulators, while retaining quantitative error guarantees rooted in kinetic theory.

## Reproducibility

We provide detailed information to facilitate the reproducibility of all numerical experiments presented in this paper. In addition to the descriptions below, the complete source code used to generate all results is publicly available at

<https://github.com/tomatofromsky/kinetic-score-landau-pinn>.

## CRedit authorship contribution statement

Minseok Kim: Software, Investigation, Validation, Visualization, Writing – original draft, Writing – review & editing. Sung-Jun Son: Software, Investigation, Validation, Writing – review & editing. Yeoneung Kim: Conceptualization, Methodology, Formal analysis, Writing – original draft, Writing – review & editing, Supervision. Donghyun Lee: Conceptualization, Methodology, Writing – review & editing, Supervision.

## Declaration of competing interest

The authors declare that they have no known competing financial interests or personal relationships that could have appeared to influence the work reported in this paper.

## Data availability

The source code used to reproduce the numerical experiments in this work is publicly available at:

<https://github.com/tomatofromsky/kinetic-score-landau-pinn>.

All datasets used in this study are synthetically generated from the prescribed initial distributions described in the paper.

## Acknowledgements

Yeoneung Kim and Minseok Kim are supported by the National Research Foundation of Korea (NRF) grant funded by the Korea government (MSIT) (RS-2023-00219980, RS-2023-00211503). Donghyun Lee and Sung-Jun Son are supported by the National Research Foundation of Korea(NRF) grant funded by the Korea government(MSIT)(No.RS-2023-00212304 and No.RS-2023-00219980). Sung-Jun Son is supported by the National Research Foundation of Korea(NRF) grant funded by the Korea government(MSIT and MOE)(No.RS-2023-00210484 and No.RS-2025-25419038).

## References

- [1] Rafael Bailo, José A. Carrillo, and Jingwei Hu. The collisional particle-in-cell method for the Vlasov–Maxwell–Landau equations. *J. Plasma Phys.*, 90(4):905900415, 2024.
- [2] C. Buet and S. Cordier. Conservative and entropy decaying numerical scheme for the isotropic Fokker-Planck-Landau equation. *J. Comput. Phys.*, 145(1):228–245, 1998.

- [3] José A. Carrillo, Matias G. Delgadino, Laurent Desvillettes, and Jeremy S.-H. Wu. The Landau equation as a gradient flow. Anal. PDE, 17(4):1331–1375, 2024.
- [4] José A. Carrillo, Matias G. Delgadino, and Jeremy Wu. Boltzmann to Landau from the gradient flow perspective. Nonlinear Anal., 219:Paper No. 112824, 49, 2022.
- [5] José Antonio Carrillo, Katy Craig, and Francesco S. Patacchini. A blob method for diffusion. Calc. Var. Partial Differential Equations, 58(2):Paper No. 53, 53, 2019.
- [6] G. Chen, L. Chacón, and D. C. Barnes. An energy- and charge-conserving, implicit, electrostatic particle-in-cell algorithm. J. Comput. Phys., 230(18):7018–7036, 2011.
- [7] P. Degond and B. Lucquin-Desreux. The Fokker-Planck asymptotics of the Boltzmann collision operator in the Coulomb case. Math. Models Methods Appl. Sci., 2(2):167–182, 1992.
- [8] Pierre Degond and Brigitte Lucquin-Desreux. An entropy scheme for the Fokker-Planck collision operator of plasma kinetic theory. Numer. Math., 68(2):239–262, 1994.
- [9] Laurent Desvillettes and Cédric Villani. On the spatially homogeneous Landau equation for hard potentials. I. Existence, uniqueness and smoothness. Comm. Partial Differential Equations, 25(1-2):179–259, 2000.
- [10] Laurent Desvillettes and Cédric Villani. On the spatially homogeneous Landau equation for hard potentials. II.  $H$ -theorem and applications. Comm. Partial Differential Equations, 25(1-2):261–298, 2000.
- [11] G. Dimarco, R. Caflisch, and L. Pareschi. Direct simulation Monte Carlo schemes for Coulomb interactions in plasmas. Commun. Appl. Ind. Math., 1(1):72–91, 2010.
- [12] Nestor Guillen and Luis Silvestre. The Landau equation does not blow up. Acta Math., 234(2):315–375, 2025.
- [13] Eero Hirvijoki. Structure-preserving marker-particle discretizations of Coulomb collisions for particle-in-cell codes. Plasma Phys. Control. Fusion, 63(4):044003, 2021.
- [14] Yan Huang and Li Wang. A score-based particle method for homogeneous Landau equation. J. Comput. Phys., 536:Paper No. 114053, 23, 2025.
- [15] Aapo Hyvärinen. Estimation of non-normalized statistical models by score matching. J. Mach. Learn. Res., 6:695–709, 2005.
- [16] Lev D. Landau. Die kinetische gleichung für den fall coulombscher wechselwirkung. Phys. Z. Sowjetunion, 10:154–164, 1936.
- [17] Lorenzo Pareschi, Giovanni Russo, and Giuseppe Toscani. Fast spectral methods for the Fokker–Planck–Landau collision operator. J. Comput. Phys., 165(1):216–236, 2000.
- [18] Maziar Raissi, Paris Perdikaris, and George E. Karniadakis. Physics-informed neural networks: A deep learning framework for solving forward and inverse problems involving nonlinear partial differential equations. J. Comput. Phys., 378:686–707, 2019.
- [19] Yang Song and Stefano Ermon. Generative modeling by estimating gradients of the data distribution. In Advances in Neural Information Processing Systems, volume 32, 2019.
- [20] Yang Song and Stefano Ermon. Improved techniques for training score-based generative models. In Advances in Neural Information Processing Systems, volume 33, pages 12438–12448, 2020.
- [21] Cédric Villani. On a new class of weak solutions to the spatially homogeneous Boltzmann and Landau equations. Arch. Ration. Mech. Anal., 143(3):273–307, 1998.
- [22] Cédric Villani. On the spatially homogeneous Landau equation for Maxwellian molecules. Math. Models Methods Appl. Sci., 8(6):957–983, 1998.

## A Proof of Theorem 6

We expand the argument in two steps.

Fix  $t \in [0, T]$  and  $\varepsilon > 0$ . Introduce the oracle KDE built from the exact characteristics  $\{v_t^{(i)}\}_{i=1}^N$ :

$$\tilde{f}_{t,N,\varepsilon}(v) := \frac{1}{N} \sum_{i=1}^N \varepsilon^{-d} K\left(\frac{v - v_t^{(i)}}{\varepsilon}\right) = \frac{1}{N} \sum_{i=1}^N K_\varepsilon(v - v_t^{(i)}), \quad K_\varepsilon(x) := \varepsilon^{-d} K(x/\varepsilon).$$

Then, by the triangle inequality and  $(a + b + c)^2 \leq 3(a^2 + b^2 + c^2)$ ,

$$\|f_{t,N,\varepsilon}^{\text{approx}} - \tilde{f}_t\|_{L_v^2}^2 \leq 3\|f_{t,N,\varepsilon}^{\text{approx}} - \tilde{f}_{t,N,\varepsilon}\|_{L_v^2}^2 + 3\|\tilde{f}_{t,N,\varepsilon} - \mathbb{E}[\tilde{f}_{t,N,\varepsilon}]\|_{L_v^2}^2 + 3\|\mathbb{E}[\tilde{f}_{t,N,\varepsilon}] - \tilde{f}_t\|_{L_v^2}^2. \quad (\text{A.1})$$

We bound each term on the right-hand side.

Since  $v_t^{(i)} \stackrel{\text{i.i.d.}}{\sim} \tilde{f}_t$ , we have  $\mathbb{E}[\tilde{f}_{t,N,\varepsilon}] = K_\varepsilon * \tilde{f}_t$ . Assume  $\tilde{f}_t \in W^{2,\infty}(\mathbb{T}^d)$  and  $K$  is symmetric with  $\int K = 1$ . A second-order Taylor expansion gives the standard bias estimate

$$\|\mathbb{E}[\tilde{f}_{t,N,\varepsilon}] - \tilde{f}_t\|_{L_v^2}^2 = \|K_\varepsilon * \tilde{f}_t - \tilde{f}_t\|_{L_v^2}^2 \leq C_{\text{bias}} \varepsilon^4, \quad (\text{A.2})$$

where  $C_{\text{bias}}$  depends only on  $\|D^2 \tilde{f}_t\|_{L_v^\infty}$  and the second moment  $\int_{\mathbb{T}^d} |u|^2 |K(u)| du$ .

Write

$$\tilde{f}_{t,N,\varepsilon}(v) - \mathbb{E}[\tilde{f}_{t,N,\varepsilon}(v)] = \frac{1}{N} \sum_{i=1}^N \left( K_\varepsilon(v - v_t^{(i)}) - \mathbb{E}[K_\varepsilon(v - V_t)] \right), \quad V_t \sim \tilde{f}_t.$$

Using independence, centering, and Fubini,

$$\mathbb{E}\|\tilde{f}_{t,N,\varepsilon} - \mathbb{E}[\tilde{f}_{t,N,\varepsilon}]\|_{L_v^2}^2 = \frac{1}{N} \mathbb{E}\left\| K_\varepsilon(\cdot - V_t) - \mathbb{E}[K_\varepsilon(\cdot - V_t)] \right\|_{L_v^2}^2 \leq \frac{1}{N} \|K_\varepsilon\|_{L_v^2}^2 = \frac{1}{N \varepsilon^d} \|K\|_{L_v^2}^2. \quad (\text{A.3})$$

Let  $e_t^{(i)} := \hat{v}_t^{(i)} - v_t^{(i)}$ . Since  $K \in C^1$  (hence  $K_\varepsilon \in C^1$ ), by the mean value theorem, for each  $i$  and each  $v$ ,

$$K_\varepsilon(v - \hat{v}_t^{(i)}) - K_\varepsilon(v - v_t^{(i)}) = - \int_0^1 \nabla_v K_\varepsilon(v - (v_t^{(i)} + s e_t^{(i)})) \cdot e_t^{(i)} ds.$$

Taking  $L_v^2$  norms and using translation invariance of  $\|\cdot\|_{L_v^2}$  yields

$$\|K_\varepsilon(\cdot - \hat{v}_t^{(i)}) - K_\varepsilon(\cdot - v_t^{(i)})\|_{L_v^2} \leq \|\nabla_v K_\varepsilon\|_{L_v^2} \|e_t^{(i)}\| = \varepsilon^{-(d/2+1)} \|\nabla_v K\|_{L_v^2} \|e_t^{(i)}\|.$$

Therefore, by Jensen and Cauchy–Schwarz,

$$\begin{aligned} \|f_{t,N,\varepsilon}^{\text{approx}} - \tilde{f}_{t,N,\varepsilon}\|_{L_v^2}^2 &= \left\| \frac{1}{N} \sum_{i=1}^N (K_\varepsilon(\cdot - \hat{v}_t^{(i)}) - K_\varepsilon(\cdot - v_t^{(i)})) \right\|_{L_v^2}^2 \\ &\leq \frac{1}{N} \sum_{i=1}^N \|K_\varepsilon(\cdot - \hat{v}_t^{(i)}) - K_\varepsilon(\cdot - v_t^{(i)})\|_{L_v^2}^2 \\ &\leq \varepsilon^{-(d+2)} \|\nabla_v K\|_{L_v^2}^2 \cdot \frac{1}{N} \sum_{i=1}^N \|e_t^{(i)}\|^2 = \varepsilon^{-(d+2)} \|\nabla_v K\|_{L_v^2}^2 E(t). \end{aligned} \quad (\text{A.4})$$

Taking expectation of (A.4) gives

$$\mathbb{E}\|f_{t,N,\varepsilon}^{\text{approx}} - \tilde{f}_{t,N,\varepsilon}\|_{L_v^2}^2 \leq \varepsilon^{-(d+2)} \|\nabla_v K\|_{L_v^2}^2 \mathbb{E}E(t).$$

Taking expectations in (A.1) and using (A.2), (A.3), and (A.4), we obtain

$$\mathbb{E}\|f_{t,N,\varepsilon}^{\text{approx}} - \tilde{f}_t\|_{L_v^2}^2 \leq C \left( \varepsilon^4 + \frac{1}{N \varepsilon^d} + \varepsilon^{-(d+2)} \mathbb{E}E(t) \right),$$

which is exactly (4.20) (absorbing the factor 3 into  $C$ ).

By the master  $W_1$ -certificate (Theorem 5) and the intermediate estimate (4.19) therein, there exists  $C(T) > 0$  such that

$$\mathbb{E}E(t) \leq C(T) \left( \int_0^t \mathbb{E} \widehat{\mathcal{E}}_{\text{ISM}}(\tau) d\tau + \int_0^t \mathbb{E} \delta_{\text{phys}}(\tau)^2 d\tau + N^{-1/2} \right). \quad (\text{A.5})$$

Substituting (A.5) into (4.20) yields (4.21) (after renaming constants). This completes the proof.

## B Experimental details

### B.1 Common Settings

Unless otherwise stated, all experiments use time step  $\Delta t = 0.01$ . For SBP and Blob baselines, the number of iterations is fixed to 25, and the learning rate is  $10^{-4}$  whenever neural networks are used. For all PINN-based models, Adam optimizer with learning rate  $10^{-4}$  is used. The activation function is SiLU.

Table 1: Training configurations across problems

Problem	$N$ SBP [14]	$N$ Blob [5]	KDE bw	$c_\gamma$
BKW 2D	22,500	22,500	0.15	1
BKW 3D	64,000	64,000	0.15	1
Anisotropic 2D	14,400	14,400	0.3	1
Rosenbluth 3D	27,000	27,000	0.3	1
Gaussian mixture 3D	64,000	64,000	0.15	1
Truncated 2D	14,400	14,400	0.3	1

For all neural networks for SBP, hidden width is 32 and depth is 3, with learning rate  $10^{-4}$ .

### B.2 PINN Architectures

All PINN experiments use  $N = 1000$  particles. The architecture consists of two networks: (i) a Particle Network and (ii) a Score Network. Both networks use SiLU activation and the Adam optimizer with learning rate  $10^{-4}$ .

**Group A: 2D Standard Configuration.** Applied to: **BKW 2D, Anisotropic 2D.**

The Particle Network uses a velocity embedding of width 32 and depth 2, a time embedding of width 16 and depth 1, followed by hidden layers of width 128 and depth 4. The Score Network uses the same architecture.

**Group B: 3D Large-Scale Configuration.** Applied to: **BKW 3D, Gaussian mixture 3D.**

The Particle Network uses a velocity embedding of width 256 and depth 2, a time embedding of width 128 and depth 1, followed by hidden layers of width 256 and depth 6. The Score Network uses the same architecture.

**Group C: Moderate 3D Configuration.** Applied to: **Rosenbluth 3D.**

The Particle Network uses a velocity embedding of width 32 and depth 2, a time embedding of width 64 and depth 1, followed by hidden layers of width 128 and depth 4. The Score Network uses a velocity embedding of width 32 and depth 2, a time embedding of width 16 and depth 1, followed by hidden layers of width 128 and depth 4.

**Group D: Mixed-Scale Configuration.** Applied to: **Truncated 2D.**

The Particle Network follows the 2D standard configuration: velocity embedding of width 32 and depth 2, time embedding of width 16 and depth 1, followed by hidden layers of width 128 and depth 4. The Score Network follows the 3D large-scale configuration: velocity embedding of width 256 and depth 2, time embedding of width 128 and depth 1, followed by hidden layers of width 256 and depth 6.

### B.3 Initial Distributions and Interaction Kernels

This appendix summarizes the initial distributions and interaction kernels used in the numerical experiments reported in Section 5. Throughout the experiments, particles are initialized by i.i.d. sampling from the prescribed initial density  $f_0$ .

**Two-dimensional BKW solution.** The analytical density is

$$\tilde{f}_t(v) = \frac{1}{2\pi K} \exp\left(-\frac{|v|^2}{2K}\right) \left(\frac{2K-1}{K} + \frac{1-K}{2K^2}|v|^2\right),$$

where  $K(t) = 1 - \frac{1}{2}e^{-t/8}$ . The associated score is available analytically via  $\tilde{s}_t(v) = \nabla_v \log \tilde{f}_t(v)$ .

**Three-dimensional BKW solution.** The density is

$$\tilde{f}_t(v) = \frac{1}{(2\pi K)^{3/2}} \exp\left(-\frac{|v|^2}{2K}\right) \left(\frac{5K-3}{2K} + \frac{1-K}{2K^2}|v|^2\right),$$

with  $K(t) = 1 - e^{-t/6}$ . These analytical solutions provide reference trajectories and scores for evaluating transport accuracy and score consistency.

**Gaussian mixture distribution** We consider a multimodal Gaussian mixture distribution in  $\mathbb{R}^3$ . The density is constructed in a separable form

$$f_0(v) = f_{0,1}(v_1) f_{0,2}(v_2) f_{0,3}(v_3),$$

where

$$\begin{aligned} f_{0,1}(v_1) &= 0.4\mathcal{N}(v_1; -2, 0.3^2) + 0.6\mathcal{N}(v_1; 1, 0.8^2), \\ f_{0,2}(v_2) &= 0.7\mathcal{N}(v_2; -1, 0.5^2) + 0.3\mathcal{N}(v_2; 2, 0.4^2), \\ f_{0,3}(v_3) &= 0.5\mathcal{N}(v_3; 0, 0.2^2) + 0.5\mathcal{N}(v_3; 3, 1.2^2). \end{aligned}$$

This construction yields a mixture with  $K = 8$  Gaussian components.

**Rosenbluth distribution** We consider the Rosenbluth-type initial distribution used in [14]:

$$f_0(v) = \frac{1}{S^2} \exp\left(-S \frac{(|v| - \sigma)^2}{\sigma^2}\right).$$

In the experiments, we use  $\sigma = 2$  and  $S = 12$ . This distribution generates a ring-shaped density in velocity space, which provides a challenging configuration for Coulomb interactions.

**Anisotropic Gaussian distribution** To test isotropization under Landau dynamics, we consider anisotropic initial data. Specifically, we use a bimodal Gaussian distribution

$$f_0(v) = \frac{1}{4\pi} \left( \exp\left(-\frac{|v - u_1|^2}{2}\right) + \exp\left(-\frac{|v - u_2|^2}{2}\right) \right),$$

where  $u_1 = (-2, 1)$  and  $u_2 = (0, -1)$ . This configuration produces two separated clusters in velocity space.

**Truncated Gaussian distribution** We consider a radially truncated Gaussian distribution in  $\mathbb{R}^2$ . Let

$$\phi_2(v) = \frac{1}{2\pi} \exp\left(-\frac{|v|^2}{2}\right)$$

denote the standard Gaussian density. The truncated density is defined by

$$f_0(v) = \frac{\phi_2(v)}{\mathbb{P}(|Z| > \eta)} \mathbf{1}_{\{|v| > \eta\}},$$

where

$$Z \sim \mathcal{N}(0, I_2).$$

Since  $|Z|$  follows a Rayleigh distribution,

$$\mathbb{P}(|Z| > \eta) = \exp(-\eta^2/2),$$

and therefore

$$f_0(v) = \frac{1}{2\pi} \exp\left(-\frac{|v|^2}{2}\right) \exp\left(\frac{\eta^2}{2}\right) \mathbf{1}_{\{|v| > \eta\}}.$$

For our experiment, we set  $\eta = 1$ .

## B.4 Discussion of Design Choices

**Dimensional scaling.** For fully three-dimensional problems with complex geometry (BKW 3D and Gaussian mixture 3D), we increase both width and depth (256, 6 layers) to enhance representation capacity. Two-dimensional problems use a lighter architecture (128, 4 layers).

**Bandwidth adjustment in Blob.** Bandwidth is set to 0.15 for near-Gaussian distributions, and increased to 0.3 for anisotropic or truncated distributions, where sharper local structures require stronger smoothing.

**Particle efficiency.** While Li–Wang and Blob require 14,400–64,000 particles depending on the problem, the PINN method consistently uses 1,000 particles. This highlights the efficiency gained from learning the score function and transport map via neural representations.